

SI Appendix.

1. Model description.

Atmosphere evolution involves many processes (Catling & Kasting 2017). This is (to our knowledge) the first paper on the transition on exoplanets from primary to secondary atmospheres. Therefore our approach is to keep the treatment of each process simple.

We consider star ages from 5 Myr, which is a typical time for nebular disk dispersal, up to 8 Gyr. We consider star masses from 0.1-1 M_{\odot} . We frequently state results for 0.3 M_{\odot} , because these are expected to be the most common host stars for worlds detected by the TESS mission (e.g. Sullivan et al. 2015, Huang et al. 2018). We emphasize planet mass 6 M_{\oplus} (bare-rock radius $\approx 1.6 R_{\oplus}$), because these are the largest (and therefore highest signal/noise) worlds that commonly have densities consistent with loss of all H_2 (Rogers 2015). The silicate mass fraction is held fixed at 2/3, with the balance consisting of the Fe/Ni metal core. This silicate mass fraction is based on Solar System data. Our results are only weakly sensitive to reasonable variations in the silicate mass fraction. The total mass of H_2 is small compared to planet mass (Lopez & Fortney 2014). The non- H_2 volatile mass fraction is also assumed to be small, consistent with data (e.g. van Eylen et al. 2018).

1a. Drivers of atmosphere loss.

Candidate drivers for the atmosphere loss that converts sub-Neptunes into super-Earths are photoevaporation, impact erosion, and core luminosity (e.g. Inamdar & Schlichting 2016, Zahnle & Catling 2017, Burger et al. 2018, Ginzburg et al. 2018, Owen & Wu 2017, Biersteker & Schlichting 2019, Kegerreis et al. 2020, Denman et al. 2020). We focus on photoevaporation in this study. Photoevaporation has been directly observed for sub-Neptune exoplanets (Bourrier et al. 2018), fits almost all of the data (e.g. Van Eylen et al. 2018), and is relatively well-understood (e.g. Murray-Clay et al. 2009). Other mechanisms are important at least for a small number of planetary systems (e.g. Owen & Estrada 2020, Loyd et al. 2020).

The rate of photoevaporation is set by the X-ray / Extreme Ultraviolet (XUV) flux, F_{XUV} (e.g. Murray-Clay et al. 2009, but see also Howe et al. 2020). XUV is generated by hot regions near the star's surface. These regions are heated by magnetic fields whose importance declines as the star sheds angular momentum, through the stellar wind, over time. Thus the star's XUV luminosity F_{XUV} declines over time. Early in a star's history, the star's XUV luminosity L_{XUV} reaches a plateau value (referred to as "saturation") of between $10^{-4}\times$ and $10^{-3}\times$ the star's total, bolometric luminosity (L).

Estimating L_{XUV} involves combining direct measurements for stars of similar spectral type and age, and interpolation over wavelength regions where star UV is absorbed by the interstellar medium. Data on L_{XUV} is synthesized by Linsky (2019). Lopez & Rice (2018) and Luger & Barnes (2015) propose power-law decays for Sun-like stars. Tu et al. (2015) quantify the variability of X-ray emission for stars of Solar mass. Guinan et al. (2016) compile L_{XUV} data for low-mass stars.

We used two approaches to interpolating in L_{XUV}/L as a function of star mass and time. In one approach, we used Figure 5 from Selsis et al. (2007) for the X-ray flux, obtaining the XUV flux from the X-ray flux using the top row of Table 4 in King et al. (2018). Selsis et al. (2007) assume a constant L_{XUV}/L of $10^{-3.2}$ during saturation. Selsis et al. (2007) do not attempt to quantify the variation of X-ray flux between stars of the same age and the same stellar mass. In the other approach, we used Jackson et al.’s (2012) fits for L_{XUV}/L for $M \geq 0.5 M_{\odot}$, patching to Guinan et al.’s (2016) fits for $M < 0.5 M_{\odot}$. We assumed that Guinan et al.’s (2016) fits applied for $M = 0.35 M_{\odot}$ and extrapolated to other M-stars. We used standard models for L and star radius (Baraffe et al. 2015) (Fig. S13). The L_{XUV}/L output from the two approaches is shown in Fig. S14. The zones of secondary atmosphere loss and revival from these approaches are shown in Fig. S9-S11. For both approaches, we also calculated how results would vary between stars of different L_{XUV}/L , assuming a 1-standard-error scatter in L_{XUV}/L of $\pm(0.4-0.5)$ dex (following Loyd et al. 2020) (Fig. 6, S16). We use an upper wavelength cutoff of 91.2 nm (13.6 eV), corresponding to the lowest-energy photon that can ionize H. However, longer-wavelength light can still contribute to atmospheric escape, especially as μ_{avg} rises. Future work using more sophisticated escape models (e.g. Wang & Dai 2018) might investigate the effect of switching on or off various UV spectral bands at lower energies than 13.6 eV.

1b. Atmosphere loss rates.

For pure- H_2 atmospheres, we set

$$dM_{\text{atm}}/dt = \varepsilon R_{\text{pl}} (R+z)^2 F_{\text{XUV}} / (G M_{\text{pl}}) \quad (\text{S1})$$

(Eqn. 6 from main text) where the heating efficiency factor, $\varepsilon = 0.15$. $\varepsilon = 0.15$ is a common choice in atmospheric evolution models. Models indicate that $\varepsilon = 0.1-0.2$ (e.g. Shematovich et al. 2014). As the planet’s atmosphere loses mass and cools, it shrinks (Lopez & Fortney 2014). This acts as a negative feedback on loss in part because smaller planets intercept fewer XUV photons. To relate the atmosphere mass M_{atm} to the planet radius ($R+z$), we used the transit-radius tables of Lopez & Fortney (2014). The homopause radius could be bigger than the transit radius by typically 5-25% (Malsky & Rogers 2020).

For our pure-high-molecular-mass atmosphere endmember loss rate, we use the loss rate in molecules/sec/cm² calculated for a pure- CO_2 atmosphere on a super-Earth by Tian (2009). This is an endmember of a high- μ_{avg} atmosphere that can self-cool efficiently. This loss rate is multiplied by μ_{avg} , and by the area of the surface-atmosphere interface, to get the loss rate in kg/s. Our intent is to bracket the likely down-shift in atmospheric loss as the atmosphere evolves to high- μ_{avg} . We extrapolate beyond the XUV-flux limits shown in Figure 6 of Tian (2009) linearly in loss rate for very large XUV fluxes, and linearly in the log of loss rate for very small XUV fluxes. High- μ_{avg} atmospheres of different composition may shed mass faster (or slower) than the pure- CO_2 case (Johnstone 2020, Johnstone et al. 2018, Zahnle et al. 2019).

For atmospheres of intermediate composition, we interpolate between the energy-limited formula ($dM_{atm}/dt \propto F_{XUV}$) to the exponential cutoff in F_{XUV} for high- μ_{avg} atmospheres ($dM_{atm}/dt \approx 0$ below a critical F_{XUV}) found by Tian (2009). Constraints for hydrodynamic loss rates of atmospheres of intermediate composition are limited (Kulikov et al. 2007, Johnstone et al. 2018). In the absence of better constraints, we use a logistic curve in \log (escape rate) and \log (mixing ratio) :

$$X_{s,atm} = (\mu_{avg} - \mu_p) / (\mu_s - \mu_p); \quad (S2)$$

$$Y = 1 / (1 + \exp(-k_1 \log_{10} X_{s,atm} - \log_{10} k_2)) \quad (S3)$$

with $k_1 = 8$ and $k_2 = 0.2$. We think that these parameter choices understate the X_{CO2} needed to suppress escape (i.e. favor the survival of high- μ atmospheres), which is conservative in terms of our conclusion that atmosphere survival is unlikely. Next we set

$$Z = \log_{10}(dM_{atm}/dt)_p - Y \log_{10} (dM_{atm}/dt)_p - \log_{10} (dM_{atm}/dt)_s \quad (S4)$$

$$(dM_{atm}/dt)_{mixed} = 10^Z \quad (S5)$$

where $(dM_{atm}/dt)_p$ is the energy-limited escape rate with $\varepsilon = 0.15$, $(dM_{atm}/dt)_s$ is from Tian (2009), and $(dM_{atm}/dt)_{mixed}$ is the loss rate for impure atmospheres.

1c. Planet thermal structure.

Planet thermal structure in our model is defined by the temperature at the atmosphere's radiative-convective boundary (T_{RCB}) and the temperature at the magma-atmosphere interface, T_{mai} . T_{RCB} and T_{mai} are related by the thickness of the convecting (adiabatic) envelope, which (in pressure units) is $(P_{atm} - P_{RCB})$, and by the adiabatic index γ (held constant at 4/3). We do not consider changes in γ with changes in atmospheric composition.

Planets form hot and cool over time. Cooling involves energy transport through the atmosphere by radiation and/or convection. If, at a given optically thick level of the atmosphere, all cooling is accomplished by radiation, then the radiative temperature gradient is

$$dT/dr = - (3 \kappa \rho / 15 \sigma T^3) (L_{int} / 4 \pi r^2) \quad (S6)$$

(e.g. Rogers et al. 2011), where κ is the local Rosseland-mean opacity, ρ is the local atmospheric density, T is local temperature, σ is the Stefan constant, and $(L_{int} / 4 \pi r^2)$ is the internal luminosity corresponding to the cooling of the planet (where r is the distance from the center of the planet). If the radiative dT/dr from Eqn. (S6) exceeds the convective adiabatic temperature gradient, then convection takes over and dT/dr is reduced to a value slightly greater than the adiabatic lapse rate. Thus, as the planet cools, and L_{int} decreases, the radiative zone expands (P_{RCB} moves to greater depths) (e.g. Bodenheimer et al. 2018,

Vazan et al. 2018). We set $P_{RCB} = 10$ bars and neglect P_{RCB} change with time, which means our magma oceans are slightly longer-lived than they would be in reality. On the other hand, we use the 1 Gyr T_{eq} value throughout the calculation, when for cool stars T_{eq} will be higher earlier in the planet’s life. This simplification tends to shorten model magma ocean lifetime relative to reality.

We assume full redistribution of energy absorbed on the dayside to the entire (4π) area of the planet. Our model planets are also isothermal with altitude above the radiative-convective boundary. In effect, we neglect the temperature difference between the planet photosphere (level at which the optical depth is approximately unity) and the radiative-convective boundary. At the top of the atmosphere we assume zero albedo. This is reasonable for cloud-free atmospheres of planets orbiting cool stars, although for Solar-mass stars the albedo will be ~ 0.2 , considering only $\text{CO}_{2(g)}$ and $\text{H}_2\text{O}_{(g)}$ opacity (Pluriel et al. 2019).

Our focus is interior to the habitable zone and for thick atmospheres. For such worlds atmospheric retention would result in magma oceans that persist for Gyr (Hamano et al. 2013, Vazan et al. 2018, Fig. S1). Thus, interior to the habitable zone, atmosphere loss is the rate-limiter for magma ocean crystallization (Hamano et al. 2013, Hamano et al. 2015, Lebrun et al. 2013). In principle our model could lead to an equilibrium situation where a few-hundred-bar high- μ atmosphere sustains a magma ocean indefinitely. However such outcomes in our model (which assumes all volatiles are delivered early) require fine-tuning.

During sub-Neptune-to-super-Earth conversion, planet cooling is driven by atmospheric removal. As the overburden pressure is removed, the remaining atmosphere cools adiabatically. This causes a temperature gradient between the magma and the atmosphere, and heat flow from the magma into the atmosphere soon warms the atmosphere because the atmosphere heat capacity is small compared to the magma ocean heat capacity. This raises T_{RCB} , and because $T_{RCB}/T_{eq} > 1$ cools the planet quickly, this cools the planet. All of these processes occur continuously in our simplified model: we assume the magma temperature tracks the loss of atmosphere. In effect we assume that convection swiftly reduces super-adiabatic temperature gradients and that the boundary layer temperature contrast at the top of the liquid magma (viscosity $< 10^{-1}$ Pa s) is small. More detailed models of sub-Neptune thermal evolution include Rogers et al. (2011), Howe & Burrows (2015), Vazan et al. (2018), and Bodenheimer et al. (2018).

For cooler orbits in our model, some crystals are present initially. This incomplete-magma-ocean initial condition is appropriate if the planet is assembled by impacts of objects that are Mars-sized or smaller (e.g. planetesimals, pebbles, or planetary embryos), and the planet cools down to the adiabat between impacts.

1d. Magma ocean crystallization.

Magma ocean crystallization shields dissolved volatiles from loss. The magma ocean crystallizes (losing mass to crystals) as the planet cools. The magma ocean mass at a given

T_{mai} depends on conditions deep within the silicate layer (higher T and much higher P than at the magma-atmosphere interface). The silicate solidus (T vs. P for 0% melt fraction) and liquidus (T vs. P for 100% melt fraction) are curved in T - P space. As a result, for a steady decline in T_{mai} , the magma mass will decrease first quickly and then slowly. To track this effect, we used the solidus, the liquidus, and the adiabat of Andraut et al. (2011) (Fig. S15). We assume that the melt fraction increases linearly with increasing temperature between the solidus and the liquidus, and neglect chemical fractionation during crystallization. We also neglect the reduction in the solidus T due to volatile enrichment as crystallization proceeds. More detailed models of magma ocean crystallization include Nikolau et al. (2019), Katyal et al. (2019), and Bower et al. (2019). Our model predicts whole mantle melting for $T_{mai} \geq 3000$ K with negligible melt below $T_{mai} \sim 1750$ K. Melting curves differ between experimenters and differ depending on assumed mantle composition (e.g. Andraut et al. 2017, Miyazaki & Korenaga 2019). To relate pressure to depth, we use the pressure-density curve from Dziewonski & Anderson (1981). To get the radius at the magma-atmosphere interface we assume $(R_{pl}/R_{\oplus}) = (M_{pl}/M_{\oplus})^{0.27}$ (Valencia et al. 2006). We integrate downward from the magma-atmosphere interface. Starting at P_{atm} and T_{mai} , we follow the adiabat until we reach the solidus. The melt mass is the mass of melt (if any) between the magma-atmosphere interface and the depth of the magma solidus. If this melt mass exceeds 2/3 of planet mass, the melt mass is set equal to 2/3 of planet mass. The effect of the weight of the atmosphere on the location of the solidus is included in our calculations, but turns out to be unimportant.

1e. Redistribution of volatiles between atmosphere, magma, and rocks.

We assume full re-equilibration between magma and atmosphere as the atmosphere is removed (efficient degassing). Degassing is efficient if the cooling magma ocean is fully convective (Ikoma et al. 2018), which can be understood as follows. Whether or not a fully liquid magma ocean undergoing whole-magma-ocean convection will degas as the H_2 envelope is removed and the liquid cools depends on (a) the number of times each magma parcel cycles through the upper thermal boundary layer during cooling, and (b) the ratio of the degassed boundary layer thickness to the thermal boundary layer thickness. Suppose the degassed boundary layer thickness is equal to the maximum depth at which bubbles can form (this assumes swift bubble ascent, and that supersaturation is unimportant). For sub-Neptune to super-Earth conversion, this is (up to 10s kbar)/ $(\rho_{magma} g) =$ up to 50 km. The thermal boundary layer thickness for a fully liquid magma ocean will be $\ll 50$ km. Each fluid parcel will go through the upper thermal boundary layer at least once during cooling.

We calculate the concentration of dissolved gas in magma using Henry's law. Many gases show linear solubility in magma. Others do not. For example, H_2O dissolves in magma in proportion to the square root of partial pressure at low p_{H_2O} , becoming more linear at high p_{H_2O} (e.g. Stolper 1982, Matsui & Abe 1986).

We adopt $s_{H_2} = 2 \times 10^{-12} \text{ Pa}^{-1}$. The basis for this is as follows. Hirschmann et al. (2012) report results from laboratory experiments on basaltic melts. Extrapolating to melts of peridotitic composition, they state that "at 1 GPa in the presence of pure H_2 , the molecular

H₂ concentration [in the melt] is 0.19 wt%.” Fegley et al. (2020, their Table 5) compile solubilities of various volatiles in molten silicates.

We ignore non-ideal solubility (due to non-ideal fugacity of the gas in the atmosphere), because it is not very important at the relatively low P_{atm} we consider (Kite et al. 2019). We also ignore joint-solubility effects because relevant data are not available. Few measurements have been made of the temperature dependence of volatile solubility in magma at $T > 2000$ K (e.g. Fegley & Schaefer 2014, Guillot & Sator 2011) and we neglect T dependence of volatile solubility.

Solid-melt distribution coefficients, D , for water partitioning into nominally anhydrous mantle minerals vary from 10^{-4} to 10^{-1} (Table S1 in Elkins-Tanton 2008), but for the most common mantle minerals are 0.02 or less. Here, “nominally anhydrous” means minerals that do not have H in their chemical formula. We use $D = 0.02$, which is at the high end of experimentally observed range (corresponding to water partitioning into pyroxene). We neglect saturation limits. C distribution coefficients are much lower, from 2×10^{-4} to 7×10^{-3} according to Elkins-Tanton (2008) and with low (1-5 ppmw) saturation limits.

1f. Magma-atmosphere coevolution.

Key initial conditions are that the quantity of the high molecular weight volatile initially in the crystal phase is zero ($s_{xtl} = 0$), and

$$e_s = C_s / (1 + (\mu_p / \mu_s)(g_{mai} / A_{mai}) m_{magma} s_s) \quad (S7)$$

which assumes that the atmosphere is dominantly p (i.e., H₂) at the zeroth timestep.

We restrict ourselves to $F/F_{\oplus} < 10^3$. For $F/F_{\oplus} > 10^3$, silicate vapor-pressure equilibrium atmospheres develop (e.g. Kite et al. 2016).

Our model loops through the following steps: (Step 1) Lose some atmosphere. → (Step 2) Post-escape outgassing. → (Step 3) Crystallize (sequestering some volatiles, but increasing the concentration of volatiles in the magma). → (Step 4) Post-crystallization outgassing → Loop back to Step 1.

Step 1. Lose atmosphere. A down-step in atmospheric pressure is prescribed. No fractionation is permitted between H₂ and the high- μ species during this escape (see section 1g). The H₂ and the high- μ species are lost in proportion to their bulk abundance in the atmosphere.

Step 2. Post-escape outgassing. The magma and atmosphere now re-equilibrate through outgassing of both H₂ and s until the partial pressures of H₂ and of s are in equilibrium with the concentrations of H₂ and s dissolved in the magma. The partial pressure of H₂ depends on the mass of H₂ in the atmosphere and on the mean molecular weight of the atmosphere, which is affected by the amount of s in the atmosphere. Similarly the partial pressure of s depends on the mass of s in the atmosphere and on the mean molecular weight of the

atmosphere, which is affected by the amount of p in the atmosphere. From Eqn. (2) in the main text, we obtain the coupled equations

$$C_s = e_s + e_s((e_s + e_p)/(e_s/\mu_s + e_p/\mu_p)) k_1/\mu_s \quad (S8)$$

$$C_p = e_p + e_p((e_s + e_p)/(e_s/\mu_s + e_p/\mu_p)) k_2/\mu_p \quad (S9)$$

where C_s (kg) is the total on-planet mass of s , C_p (kg) is the total on-planet mass of H_2 (p), e_s is the kg of s in the atmosphere, e_p is the kg of H_2 in the atmosphere, the second term on the right-hand-side of (S8) is the mass (kg) of s dissolved in the magma, the second term on the right-hand-side of (S9) is the mass (kg) of H_2 dissolved in the magma, μ_s is the molecular weight of s , μ_p is the molecular weight of H_2 , and

$$k_1 = (g_{mai}/A_{mai}) m_{magma} S_s \quad (S10)$$

$$k_2 = (g_{mai}/A_{mai}) m_{magma} S_p \quad (S11)$$

where g_{mai} and A_{mai} are (respectively) the gravity at, and area of, the magma-atmosphere interface for $(R_{mai}/R_{\oplus}) = (M_{pl}/M_{\oplus})^{0.27}$, m_{magma} is calculated as described in section 1d above, S_s is the solubility of s in the magma, and S_p is the solubility of H_2 in the magma.

The simultaneous equations (S10)-(S11) have two solutions, and the physical solution is

$$e_p = (C_p k_1 + C_s k_2 + (k_2 (C_p k_1 \mu_s - k_1 (C_p^2 k_1^2 \mu_p^2 + 2 C_p^2 k_1 \mu_p \mu_s + C_p^2 \mu_s^2 + 2 C_p C_s k_1 k_2 \mu_p \mu_s - 2 C_p C_s k_1 \mu_p^2 + 4 C_p C_s k_1 \mu_p \mu_s + 4 C_p C_s k_2 \mu_p \mu_s - 2 C_p C_s k_2 \mu_s^2 + 2 C_p C_s \mu_p \mu_s + C_s^2 k_2^2 \mu_s^2 + 2 C_s^2 k_2 \mu_p \mu_s + C_s^2 \mu_p^2)^{0.5} - C_s k_1 \mu_p + 2 C_s k_2 \mu_s + C_p k_1^2 \mu_p + C_s k_1 k_2 \mu_s)) / (2 (k_1 \mu_p - k_2 \mu_s + k_1^2 \mu_p - k_1 k_2 \mu_s)) + (k_1 k_2 (C_p k_1 \mu_s - k_1 (C_p^2 k_1^2 \mu_p^2 + 2 C_p^2 k_1 \mu_p \mu_s + C_p^2 \mu_s^2 + 2 C_p C_s k_1 k_2 \mu_p \mu_s - 2 C_p C_s k_1 \mu_p^2 + 4 C_p C_s k_1 \mu_p \mu_s + 4 C_p C_s k_2 \mu_p \mu_s - 2 C_p C_s k_2 \mu_s^2 + 2 C_p C_s \mu_p \mu_s + C_s^2 k_2^2 \mu_s^2 + 2 C_s^2 k_2 \mu_p \mu_s + C_s^2 \mu_p^2)^{0.5} - C_s k_1 \mu_p + 2 C_s k_2 \mu_s + C_p k_1^2 \mu_p + C_s k_1 k_2 \mu_s)) / (2 (k_1 \mu_p - k_2 \mu_s + k_1^2 \mu_p - k_1 k_2 \mu_s))) / (k_1 + k_1 k_2) \quad (S12)$$

$$e_s = -(C_p k_1 \mu_s - k_1 (C_p^2 k_1^2 \mu_p^2 + 2 C_p^2 k_1 \mu_p \mu_s + C_p^2 \mu_s^2 + 2 C_p C_s k_1 k_2 \mu_p \mu_p - 2 C_p C_s k_1 \mu_p^2 + 4 C_p C_s k_1 \mu_p \mu_s + 4 C_p C_s k_2 \mu_p \mu_s - 2 C_p C_s k_2 \mu_s^2 + 2 C_p C_s \mu_p \mu_s + C_s^2 k_2^2 \mu_s^2 + 2 C_s^2 k_2 \mu_p \mu_s + C_s^2 \mu_p^2)^{0.5} - C_s k_1 \mu_p + 2 C_s k_2 \mu_s + C_p k_1^2 \mu_p + C_s k_1 k_2 \mu_s) / (2 (k_1 \mu_p - k_2 \mu_s + k_1^2 \mu_p - k_1 k_2 \mu_s)) \quad (S13)$$

We recalculate the other variables by inserting the new e_s and e_p into Eqns. (S8) and (S9).

The coupling of Eqn. (S8) and Eqn. (S9) via μ_{avg} has two important effects that disfavor secondary atmospheres on exoplanets. During the loss of the primary atmosphere, the μ_{avg} effect increases the amount of the high- μ constituent in the atmosphere by a factor of 15 ($= \mu_s/\mu_p$), increasing the amount of the high- μ constituent that is lost to space. Moreover, as μ_{avg} rises from 2 to 30, because the partial pressure of the high- μ constituent scales with the number ratio of s in the atmosphere, $f_s = e_s / (e_p + e_s)(\mu_{avg}/\mu_p)$, the number of moles of s in the atmosphere for a given saturation vapor pressure of s decreases by a factor of 15

($= \mu_s/\mu_p$). This negative feedback reduces the number of worlds that smoothly transition from a primary to a secondary atmosphere.

Step 3. Crystallize. The magma mass is forced to a lower value, consistent with the lower T_{mai} associated with the atmospheric pressure that was reduced in Step 1. The freshly-produced crystals gain an s concentration (in mass fraction) of $D_s \times X_s$, where X_s is the mass fraction of the volatile in the magma. The crystals are not remixed (by assumption) on the timescale of magma-ocean crystallization. s within crystals is relatively safe from release into the unsafe surface environment during sub-Neptune-to-super-Earth conversion, because solid-state creep speeds within the solid mantle are $10^{-9} - 10^{-8} \text{ m s}^{-1}$, versus up to 10^1 m s^{-1} in the magma. As a result, the concentration of the crystals is independent of the previous partitioning of the volatiles into the solid rock. Partitioning of H_2 into the crystals is not considered.

Step 4. Post-crystallization outgassing. Because $D_s < 1$, the magma ocean is enriched in s after the crystallization step. Therefore we re-equilibrate the magma and the atmosphere taking account of the now-higher concentration of s (X_s) in the magma.

The processes involved in Steps 1-4 all occur on timescales short compared to the magma ocean lifetime.

1g. Calculating evolution over time.

To map the rocky planet evolution sequence onto time we combine the environmental drivers from (1a), the loss rates from (1b), and the small planet evolution sequence from (1f). T_{RCB} is fixed in the crystallization calculation, but T_{eq} evolves with star age. We deal with this by setting T_{RCB} throughout the calculation equal to T_{eq} at a fixed age of 1 Gyr. Thus, planets orbiting cool stars in our model have shorter-lived magma oceans than in reality.

Diffusive separation of H_2 from high- μ species is important at lower XUV flux (e.g. Hu et al. 2015, Wordsworth et al. 2018, Saito & Kuramoto 2018, Odert et al. 2018, Malsky & Rogers 2020). However, diffusive separation is washed out at the high XUV fluxes required if photoevaporation is to cause sub-Neptune-to-super-Earth conversion (Tian 2015, Catling & Kasting 2017). To demonstrate this, we first define the (atomic) H flux, F_1 , on the assumption that the overwhelming majority of the upper atmosphere is comprised of H:

$$F_1 = \varepsilon F_{\text{XUV}} (R + z) / (4 G M_{pl} m_1) \quad (\text{S14})$$

in units of molecules $\text{s}^{-1} \text{ m}^{-2}$. Here, $\varepsilon = 0.15$ is the efficiency of conversion of XUV energy into atmospheric escape, R is solid-planet radius, z is atmosphere thickness (which we set to $0.4 R$ to correspond to a small sub-Neptune), G is the gravitational constant, M_{pl} is planet mass, and m_1 is the mass (kg) of the hydrogen atom.

From this we obtain the crossover mass m_c (Tian 2015)

$$m_c = m_1 + k T F_1 / (b g X_1) \quad (\text{S15})$$

where T is the temperature of the heterosphere, and $b = 4.8 \times 10^{19} T^{0.75} \text{ m}^{-1} \text{ s}^{-1}$ is the binary diffusion coefficient, corresponding to neutral H and neutral O, used by Tian (2015). Including the effect of ionization of H would decrease the effective value of b (Hu et al. 2015) and so strengthen our conclusion that diffusive separation is not important during sub-Neptune to super-Earth conversion for *Kepler's* super-Earths. We set $T = 10^4 \text{ K}$, the same value used by Hu et al. (2015) and Malsky & Rogers (2020).

The flux, F_2 , of the high- μ species is zero when $m_c < m_2$. When $m_c > m_2$ the flux F_2 is given by

$$F_2 = F_1 (X_2 (m_c - m_2)) / (X_1 (m_c - m_1)) \quad (\text{S16})$$

Substituting in values for $6 M_\oplus$ and atomic mass 15 Da we find $F_{\text{XUV}} = 0.7 \text{ W/m}^2$ at crossover, 1.3 W/m^2 for 50% reduction in escaping flux due to weight differences, and 6.1 W/m^2 for escaping flux of high-molecular weight species at 90% of the flux if there was no fractionation at all. All three thresholds are shown as dashed vertical lines on Fig. S5 and Fig. S6. In the context of sub-Neptune to super-Earth conversion, most of the atmosphere mass is removed at higher F_{XUV} . Most exoplanets either stay as sub-Neptunes or lose their atmosphere too quickly for the XUV flux to drop to levels that permit >10% differences in loss rate due to fractionation. This can be understood as follows. If the upper atmosphere absorbs 1 W/m^2 of light from the star, the upper limit on loss rate for a $6 M_\oplus$ world is $\sim 10 \text{ bars/Myr}$, falling to 1.5 bars/Myr at $\varepsilon = 0.15$. Since sub-Neptune-to-super-Earth conversion takes $\sim 300 \text{ Myr}$, and $\sim 5 \times 10^4 \text{ bars}$ of H_2 need to be removed (including H_2 that is initially dissolved in the magma), F_{XUV} must be $\sim 100 \text{ W/m}^2$. Using the saturation threshold of Selsis et al. (2007), ($F_{\text{XUV}}/F = 10^{-3.2}$) this corresponds to 160 kW/m^2 , $F/F_\oplus = 120$, for distance from the star = 0.1 AU for a Sun-like star. This is the typical distance of a *Kepler* super-Earth from its host star (the abundance of $1.6 R_\oplus \sim 6 M_\oplus$ super-Earths drops off rapidly at larger separations (Fulton et al. 2017, Fulton & Petigura 2018)). At such high XUV fluxes, fractionation causes negligible differences in the loss rate relative to the no-fractionation case. Therefore, our approximation of no fractionation during sub-Neptune to super-Earth conversion is valid.

However, fractionation by diffusion can be important for the composition of late-stage volcanically outgassed atmospheres. For example, the volcanic H_2 outgassing flux is calculated to be less than the diffusively-limited H_2 escape rate unless H_2 stays at a very low level (e.g. Catling et al. 2001, Batalha et al. 2016, Zahnle et al. 2019). We expect that this effect would maintain volcanically outgassed atmospheres at high μ_{avg} , even if outgassing of H_2 by serpentinization (Sleep et al. 2004) and/or volcanic outgassing is large.

Fractionation by diffusion is also much more important for Habitable Zone super-Earth-sized planets. For $F_{\text{bol}} = 1361 \text{ W/m}^2$ (the Solar flux at 1 AU today), even at saturation F_{XUV} is 0.9 W/m^2 , which is only marginally capable of lifting atomic mass = 15 Da species out of the atmosphere. This favors the occurrence of secondary atmospheres on Habitable Zone exoplanets.

Finally, exposure to moderate F_{XUV} for Gyr may convert a H_2 -dominated sub-Neptune atmosphere into a He-enriched sub-Neptune, provided the planet does not start with too much H_2 (Hu et al. 2015, Malsky & Rogers 2020).

1h. Volcanic outgassing.

No exoplanets have yet been confirmed to be volcanically active. We use a simple model of the geodynamics and rate of volcanism on super-Earth-sized planets (Kite et al. 2009). The model includes parameterized mantle convection, thermal evolution, and volcanism for both plate tectonics and stagnant lid modes. The model is tuned to reproduce Earth’s present-day rate of volcanism in plate tectonics mode. Kite et al. (2009) consider three different melting models. In the present study, we use the results from the widely-used melting model of Katz et al. (2003). Many more sophisticated models of rocky exoplanet thermal evolution, geodynamics, and volcanic activity exist (e.g. Dorn et al. 2018, and references therein).

The procedure for estimating the rate of volcanism starts from the results of Kite et al. (2009) (Fig. S3). This is an Earth-tuned parameterized mantle convection and rate of volcanism model that predicts the rate of volcanism versus time for either stagnant lid mode and plate tectonics mode. The rate of CO_2 release at Earth’s mid-ocean ridges (12 ± 2 bars/Gyr; Tucker et al. 2018) is multiplied by the computed rate of volcanism, in units of Earth’s present-day rate, to obtain the predicted rate of CO_2 release on the rocky exoplanet. This is adjusted downward in proportion to any early loss of high-molecular-weight volatiles to space. For example, if a model exoplanet has lost 70% of its high-molecular-weight volatiles to space, then the rate of volcanic outgassing is reduced to 30% of the volumetric volcanic flux predicted from the Earth-tuned model of Super-Earth volcanism.

Fig. 6 compares the broad zone of worlds with atmosphere for planets that form without thick H_2 atmospheres to the much more restricted zone of volcanically revived atmospheres for worlds that form with thick H_2 atmospheres. This calculation assumes that half of worlds form with $s_s = 10^{-9} \text{ Pa}^{-1}$ (for which $\sim 90\%$ of high- μ volatiles are lost to space during the loss of the H_2 -dominated atmosphere), and half form with $s_s = 10^{-11} \text{ Pa}^{-1}$. Atmospheric ingassing is neglected because worlds well inside the habitable zone are too hot for weathering reactions to sequester atmophiles in the crustal rocks. Volatile release by volcanic outgassing is neglected, by construction, on worlds that start with all their volatiles in the atmosphere. Forming with a secondary atmosphere is advantageous for subsequently exhibiting a secondary atmosphere, relative to the total-loss-and-subsequent-revival process. The stagnant-lid and plate-tectonics predictions diverge greatly after ~ 4 Gyr, when volcanism shuts down on the stagnant-lid model planet (Fig. S8). The plate-tectonics and stagnant lid predictions otherwise appear similar in this Earth-scaled model (Kite et al. 2009). However, this overall similarity of plate and stagnant-lid predictions is specific to the Earth-tuned model of Kite et al. (2009): at least one other model predicts much stronger suppression of volcanism on stagnant-lid super-Earth-sized rocky planets (e.g. Dorn et al. 2018). Tidal locking, by itself, has little effect on volcanism (e.g. van Summeren et al. 2011). So long as we do not mechanistically understand

volcanism versus time for Solar System worlds (Byrne et al. 2019), why Earth’s mantle took so long to mix, nor why Earth’s mantle is not yet completely outgassed, we think that it is appropriate to use basic models to predict rate of volcanism versus time for rocky exoplanets. A robust constraint (for non-tidally-heated planets) is decline of mantle temperature by 50-200K per Gyr, with a concomitant decline in the potential for melting (Stevenson 2003).

We assume the rate of degassing is proportional to the rate of magmatism. This is a simplification. Even low-degree partial melts can effectively extract almost all the volatiles from the full mass of silicate mantle that sweeps through the partial melt zone. This is because volatiles partition strongly into the melt during partial melting (i.e., $D_i \ll 1$). Once the partial melt fraction is high enough ($\sim 1\%$) for the melt to form interconnected channels, the volatile bearing melt rises from the melt production zone geologically instantaneously (with no loss of volatiles) via filter-pressing, melt channel formation, and diking. Whether the melt gets close enough to the surface to form bubbles and/or erupt explosively will depend on the stress state of the lithosphere (e.g. Solomon 1978). Explosive volcanic eruptions are aided by bubble formation, which is easier when the volatile content of the magma is high. If melt crystallizes at depth (intrusion) then volatiles will go into hydrated minerals or into the glass phase, where they might still be released to the atmosphere over geologic time.

Extrapolation of simple models of Earth’s thermal evolution and outgassing rate back into Earth’s past leads to the expectation that Earth’s mantle was very rapidly stirred and quickly outgassed very early in Earth history – in contradiction to isotopic data that show sluggish stirring. Similarly, our simple Earth-tuned model of thermal evolution and outgassing rate indicates that 4-6 \times more volatiles outgas over the lifetime of the planet than are present at the beginning – a mass balance violation. Because an excess of volcanism over XUV-driven atmospheric loss leads (in our model) to build-up of a detectable atmosphere in <1 Gyr, the rate of volcanism is more important than the cumulative amount of volcanism in setting atmosphere presence/absence. Therefore we do not adjust our volcanic fluxes downward to take account of this effect, reasoning that real planets outgas more slowly than simple models predict. Alternatively, our results could be interpreted as saying that super-Earths erupt away their solid-mantle volatiles during the first Gyr of the star’s life, when XUV fluxes are still high. This would lead to an even more unfavorable conclusion for the likelihood of volcanically outgassed atmospheres at distances much closer to the star than the habitable zone than is presented in Fig. 6.

To calculate the atmosphere presence/absence lines shown in Fig. 6 and Fig. S16, we varied following parameters. (1) XUV flux: multiplied by a factor drawn randomly from a lognormal distribution centered on 1 and with a standard deviation of 0.4 dex (Lyon et al. 2019). (2) Earth CO₂ outgassing rate: a quantity drawn randomly from a normal distribution centered on 0 and with a standard deviation of 2 bars/Gyr is added to the nominal value of 12 bars/Gyr. (3) Solubility of the high-molecular-weight species in the magma: alternated between values of 10^{-11} Pa⁻¹ and 10^{-9} Pa⁻¹. We used 1 bar atmospheric pressure as the threshold for atmosphere presence/absence.

The model results are more sensitive to changes in the XUV flux than they are to changes in the rate of volcanic outgassing. This is due to the exponential cutoff in the XUV-flux-driven loss rate of CO₂ (Tian 2009).

1i. Supply and observability.

The inventory of CO₂ even on today's Earth is uncertain. For example, the review of Lee et al. (2019) reports a range of estimates for the C stored in the non-sedimentary rocks of Earth's continental crust, from 4.2×10^7 Gton C to 2.6×10^8 Gton C. This increases the likelihood that some hot rocky exoplanets have C inventories large enough to retain an observable atmosphere.

No exoplanets have yet been confirmed to contain >1 wt% H₂O. Modeling papers tracking the formation, migration, and (for habitable-zone worlds) climate evolution of worlds with >1 wt% H₂O include Kite & Ford (2018), Bitsch et al. (2019), and references therein.

Another way to increase volatile mass is to ballast the hydrogen with oxygen obtained from the reaction $\text{FeO}_{(\text{magma})} + \text{H}_{2(\text{g})} \rightarrow \text{Fe} + \text{H}_2\text{O}_{(\text{g})}$; i.e., endogenic water which does not require planet migration (Kite et al. 2020).

SI References.

Andrault, D., Bolfan-Casanova, N., Nigro, G. L., et al. 2011, Solidus and liquidus profiles of chondritic mantle: Implication for melting of the Earth across its history, *Earth Planet. Sci. Lett.*, 304, 251.

Andrault, D., Bolfan-Casanova, N., Bouhifd, M. A., et al. 2017, Toward a coherent model for the melting behavior of the deep Earth's mantle, *Phys. Earth & Planet Interiors*, 265, 67.

Baraffe, I., et al. 2015, New evolutionary models for pre-main sequence and main sequence low-mass stars down to the hydrogen-burning limit, *Astronomy & Astrophysics*, Volume 577, id.A42.

Batalha, N., Kopparapu, R. K., Haqq-Misra, J. & Kasting, J. F., 2016, Climate cycling on early Mars caused by the carbonate–silicate cycle, *Earth Planet. Sci. Lett.* 455, 7–13.

Biersteker, J. B., & Schlichting, H. E. 2019, Atmospheric mass-loss due to giant impacts: the importance of the thermal component for hydrogen–helium envelopes, *Monthly Notices of the Royal Astronomical Society*, 485, 4454.

Bitsch, B., et al., 2019, *Astronomy & Astrophysics*, Volume 624, id.A109, 12 pp.

Bodenheimer, P., Stevenson, D. J., Lissauer, J. J., & D'Angelo, G. 2018, New Formation Models for the Kepler-36 System, *Astrophysical Journal*, 868, 138.

Bourrier, V., et al., 2018, Hubble PanCET: an extended upper atmosphere of neutral hydrogen around the warm Neptune GJ 3470b, *Astronomy & Astrophysics*, 620, A147.

Bower, D.J., et al., 2019, Linking the evolution of terrestrial interiors and an early outgassed atmosphere to astrophysical observations, *Astronomy & Astrophysics*, 631, id.A103, 18 pp.

Burger, C., et al., 2018, Transfer, loss and physical processing of water in hit-and-run collisions of planetary embryos, *Celestial Mechanics and Dynamical Astronomy* 130, art. no. 2.

Byrne, P.K., 2019, A comparison of inner Solar System volcanism, *Nature Astronomy*, doi:10.1038/s41550-019-0944-3.

Catling, D. C., & Kasting, J. F. 2017, *Atmospheric Evolution on Inhabited and Lifeless Worlds* (Cambridge: Cambridge Univ. Press).

Catling, D.C., K. J. Zahnle, and C. P. McKay, Biogenic methane, hydrogen escape, and the irreversible oxidation of early Earth, *Science*, 293, 839-843, 2001.

Denman, T.R., et al., Atmosphere loss in planet-planet collisions, arXiv:2006.01881.

Dorn, C., et al., 2018, Outgassing on stagnant-lid super-Earths, *Astronomy & Astrophysics*, 614, A18.

Dziewonski, A. M., & Anderson, D. L. 1981, Preliminary reference Earth model, *Phys. Earth Planet. Int.*, 25, 297.

Elkins-Tanton 2008, Linked magma ocean solidification and atmospheric growth for Earth and Mars, *Earth and Planetary Science Letters* 271, 181-191.

Fegley, B., et al., 2020, Volatile element chemistry during accretion of the Earth, *Geochemistry: Chemie der Erde*, 80(1), 125594.

Fegley, B., & L. Schaefer, 2014, Chemistry of the Earth's Earliest Atmosphere. *Treatise on Geochemistry*, 2nd edition, chapter 6.3.

Fulton, B. J., Petigura, E. A., Howard, A. W., et al. 2017, The California-Kepler Survey. III. A Gap in the Radius Distribution of Small Planets, *AJ*, 154, 109.

Fulton, B. J., & Petigura, E. A. 2018, The California-Kepler survey. VII. Precise planet radii leveraging Gaia DR2 reveal the stellar mass dependence of the planet radius gap, *Astronomical Journal*, 156, 264.

Ginzburg, S., et al., Super-Earths, *in* Formation, Evolution, and Dynamics of Young Solar Systems, *Astrophys. & Space Sci. Library*, v.445, edited by M. Pessah & O. Gressel, Springer.

Guillot B. & N. Sator 2011, Carbon dioxide in silicate melts: A molecular dynamics simulation study, *GCA* 75, 1829-1857.

Guinan et al. 2016, Living with a red dwarf: rotation and X-ray and ultraviolet properties of the halo population Kapteyn's star, *Astrophysical Journal*, 821, article id. 81.

Hamano, K., et al. 2013, Emergence of two types of terrestrial planet on solidification of magma ocean, *Nature*, 497, 607-610.

Hamano, K. et al. 2015, Lifetime and spectral evolution of a magma ocean with a steam atmosphere: its detectability by future direct imaging, *Astrophysical Journal*, 806, article id. 216.

Hirschmann, M.M., et al. 2012, Solubility of molecular hydrogen in silicate melts and consequences for volatile evolution of terrestrial planets, *Earth and Planetary Science Letters* 345, 38-48.

- Howe, A. R., & Burrows, A. 2015, Evolutionary models of super-Earths and mini-Neptunes incorporating cooling and mass loss, *Astrophysical Journal*, 808, 150.
- Howe, A., F. Adams and M. Meyer 2020, Survival of Primordial Planetary Atmospheres: Photodissociation Driven Mass Loss, *Astrophysical Journal* 894:130.
- Hu, R., et al. 2015, Helium atmospheres on warm Neptune-and sub-Neptune-sized exoplanets and applications to GJ 436b, *Astrophysical Journal*, 807:8.
- Huang, C. X., Burt, J., Vanderburg, A., et al. 2018, TESS Discovery of a Transiting Super-Earth in the pi Mensae System, *Astrophysical Journal*, 868, L39
- Ikoma, M., Elkins-Tanton, L., Hamano, K., Suckale, J. 2018. Water partitioning in planetary embryos and protoplanets with magma oceans, *Space Sci. Rev.* 214, 76.
- Inamdar, N. K., Schlichting, H. E. 2016. Stealing the gas: giant impacts and the large diversity in exoplanet densities, *Astrophysical Journal* 817, L13.
- Jackson, A.P., Davis, T.A., & Wheatley, P.J., 2012, The coronal X-ray-age relation and its implications for the evaporation of exoplanets, *Monthly Notices of the Royal Astronomical Society*, 422, 2024-2043.
- Johnstone, C. et al. 2018, Upper atmospheres of terrestrial planets: Carbon dioxide cooling and the Earth's thermospheric evolution, *Astronomy & Astrophysics*, 617, id.A107.
- Johnstone, C. 2020, Hydrodynamic Escape of Water Vapor Atmospheres near Very Active Stars, *Astrophysical Journal*, 890, id.79.
- Katyal, N., et al. 2019, Evolution and Spectral Response of a Steam Atmosphere for Early Earth with a Coupled Climate-Interior Model, *Astrophysical Journal* 875:31
- Katz, R. F., Spiegelman, M., & Langmuir, C. H. 2003, A new parameterization of hydrous mantle melting, *Geochem. Geophys. Geosyst.* 4, 1073.
- Kegerreis, J.A., et al., 2020, Atmospheric Erosion by Giant Impacts onto Terrestrial Planets, *arXiv:2002.02977*.
- King, G.W., et al., 2018, The XUV environments of exoplanets from Jupiter-size to super-Earth, *Monthly Notices of the Royal Astronomical Society*, 478, 1193-1208.
- Kite, E. S., Manga, M., & Gaidos, E. 2009, Geodynamics and rate of volcanism on massive Earth-like planets, *Astrophysical Journal*, 700, 1732.
- Kite, E. S., Fegley, B., Jr., Schaefer, L., & Gaidos, E. 2016, Atmosphere-interior exchange on hot, rocky exoplanets, *Astrophysical Journal*, 828, 80.
- Kite, E.S., & Ford, E.B., 2018, Habitability of exoplanet waterworlds, *Astrophysical Journal*, 864, 75.
- Kite, E. S., Fegley, B., Schaefer, L., & Ford, E. B., 2019, Superabundance of exoplanet sub-Neptunes explained by fugacity crisis, *Astrophysical Journal*, 87, L33.
- Kite, E. S., Fegley, B., Schaefer, L., & Ford, E. B., 2020, Atmosphere origins on exoplanet sub-Neptunes, *Astrophysical Journal*, 891, 111.
- Kulikov et al. 2007, A comparative study of the influence of the active young Sun on the early atmospheres of Earth, Venus, and Mars, *Space Science Reviews*, 129, 207-243.

- Lebrun, T., et al. 2013, Thermal evolution of an early magma ocean in interaction with the atmosphere, *J. Geophys. Res.-Planets* 118, 1155-176.
- Lee, C., Jiang, H., Dasgupta, R., & Torres, M. (2019). A Framework for Understanding Whole-Earth Carbon Cycling. In B. Orcutt, I. Daniel, & R. Dasgupta (Eds.), *Deep Carbon: Past to Present* (pp. 313-357). Cambridge: Cambridge University Press.
- Linsky, J., 2019, *Host Stars and their Effects on Exoplanet Atmospheres*, Springer.
- Lopez, E., & Fortney, J., 2014, Understanding the mass-radius relation for sub-Neptunes: Radius as a proxy for composition, *Astrophysical Journal* 721:1.
- Lopez, E. D., & Rice, K. 2018, How formation time-scales affect the period dependence of the transition between rocky super-Earths and gaseous sub-Neptunes and implications for η_{\oplus} , *Monthly Notices of the Royal Astronomical Society*, 479, 5303-5311.
- Lloyd, R.O.P., et al., 2020, Current Population Statistics Do Not Favor Photoevaporation over Core-powered Mass Loss as the Dominant Cause of the Exoplanet Radius Gap, *Astrophysical Journal* 890:23.
- Luger, R. & Barnes 2015, Extreme water loss and abiotic O₂ buildup on planets throughout the habitable zones of M dwarfs, *Astrobiology*, 15(2), 119-143.
- Malsky, I., & L. Rogers 2020, Coupled Thermal and Compositional Evolution of Photo Evaporating Planet Envelopes, *Astrophysical Journal*, 896:48.
- Mansfield, M. et al. 2019, Identifying Atmospheres on Rocky Exoplanets through Inferred High Albedo, *Astrophysical Journal* , 886:141.
- Matsui, T. & Y. Abe, 1986, Evolution of an impact-induced atmosphere and magma ocean on the accreting Earth, *Nature* 319, 303–305
- Miyazaki, Y., & Korenaga, J. 2019, On the timescale of magma ocean solidification and its chemical consequences: 2. Compositional differentiation under crystal accumulation and matrix compaction, *J. Geophys. Res. (Solid Earth)*, 124, 3399
- r-Clay, R., et al. 2009, Atmospheric escape from hot Jupiters, *ApJ* 693, 23-42.
- Nikolaou et al. 2019, What factors affect the duration and outgassing of the terrestrial magma ocean?, *Astrophysical Journal* 875:11.
- Odert, P., et al., 2018, Escape and fractionation of volatiles and noble gases from Mars-sized planetary embryos and growing protoplanets, *Icarus* 307, 327-346.
- Owen, J., & B. C. Estrada 2020, Testing exoplanet evaporation with multitransiting systems, *Monthly Notices of the Royal Astronomical Society*, 491, 5287-5297.
- Owen, J. E., & Wu, Y. 2017, The evaporation valley in the Kepler planets, *Astrophysical Journal*, 847, 29.
- Otegi, J.F., et al. 2019, Revisited mass-radius relations for exoplanets below 120 M_{\oplus} , *Astronomy & Astrophysics*, 643, A43.
- Pluriel, W., et al. 2019, Modeling the albedo of Earth-like magma ocean planets with H₂O-CO₂ atmospheres, *Icarus* 317, 583-590.
- Rogers, L.A., 2015, Most 1.6 Earth-radius Planets are Not Rocky, *Astrophysical Journal*, 801, article id. 41.

- Rogers, L. A., Bodenheimer, P., Lissauer, J. J., Seager, S. 2011, Formation and structure of low-density exo-Neptunes, *Astrophysical Journal*, 738, 59.
- Saito, H., & K. Kuramoto, 2018, Formation of a hybrid-type proto-atmosphere on Mars accreting in the solar nebula, *Monthly Notices of the Royal Astronomical Society*, 475, 1274-1287.
- Selsis, F., et al., 2007, Habitable planets around the star Gliese 581?, 476, 1373-1387.
- Shematovich, V. I., Ionov, D. E., & Lammer, H. 2014, Heating efficiency in hydrogen-dominated upper atmospheres, *Astronomy & Astrophysics*, 571, A94.
- Sleep, N., et al., 2004, H₂-rich fluids from serpentinization: geochemical and biotic implications, *PNAS* 101, 12818-12823.
- Solomon, S.C. 1978, On volcanism and thermal tectonics on one-plate planets, *Geophysical Research Letters*, 5, 461-464.
- Stevenson, D.J., 2003, Styles of mantle convection and their influence on planetary evolution, *Comptes Rendus Geoscience*, 335, 99-111.
- Stolper, E. 1982, The speciation of water in silicate melts, *Geochimica et Cosmochimica Acta*, 46, 2609.
- Sullivan, P.W., et al., 2015, The Transiting Exoplanet Survey Satellite: Simulations of Planet Detections and Astrophysical False Positives, *The Astrophysical Journal*, 809, article id. 77, 29 pp.
- Tian, F. 2009, Thermal escape from super Earth atmospheres in the habitable zones of M stars, *Astrophysical Journal* L 703:905-909
- Tian, F., et al. 2009, Thermal escape of carbon from the early Martian atmosphere, *GRL* 36, L02205, doi:10.1029/2008GL036513.
- Tian, F. 2015, History of water loss and atmospheric O₂ buildup on rocky exoplanets near M dwarfs, *EPSL*, 432, p. 126-132.
- Tu, L., et al., 2015, The extreme ultraviolet and X-ray Sun in Time: High-energy evolutionary tracks of a solar-like star, *Astronomy & Astrophysics* 577, L3.
- van Summeren, J., Conrad, C. P., & Gaidos, E. 2011, Mantle convection, plate tectonics, and volcanism on hot exo-Earths, *Astrophysical Journal Letters*, 736, L15
- Valencia, D., O'Connell, R. J., & Sasselov, D. 2006, Internal structure of massive terrestrial planets, *Icarus*, 181, 545.
- Van Eylen, V., Agentoft, C., Lundkvist, M. S., et al. 2018, An asteroseismic view of the radius valley: stripped cores, not born rocky, *Monthly Notices of the Royal Astronomical Society*, 479, 4786.
- Vazan, A., Ormel, C. W., Noack, L., Dominik, C. 2018. Contribution of the core to the thermal evolution of sub-Neptunes, *Astrophysical Journal*, 869, 163.
- Wang, L., & F. Dai, 2018, Evaporation of Low-mass Planet Atmospheres: Multidimensional Hydrodynamics with Consistent Thermochemistry, *Astrophysical Journal*, 860:175.

Wordsworth, R.D., et al. 2018, Redox evolution via gravitational differentiation on low-mass planets: Implications for abiotic oxygen, water loss, and habitability, *Astromical Journal*, 155:195.

Zahnle, K., & D. Catling 2017, The cosmic shoreline: The evidence that escape determines which planets have atmospheres, and what this may mean for Proxima Centauri b, *Astrophysical Journal*, 843:122

Zahnle, K., et al. 2019, Strange messenger: A new history of hydrogen on Earth, as told by Xenon, *Geochim. Cosmichim. Acta* 244, 56-85.

SI Figures.

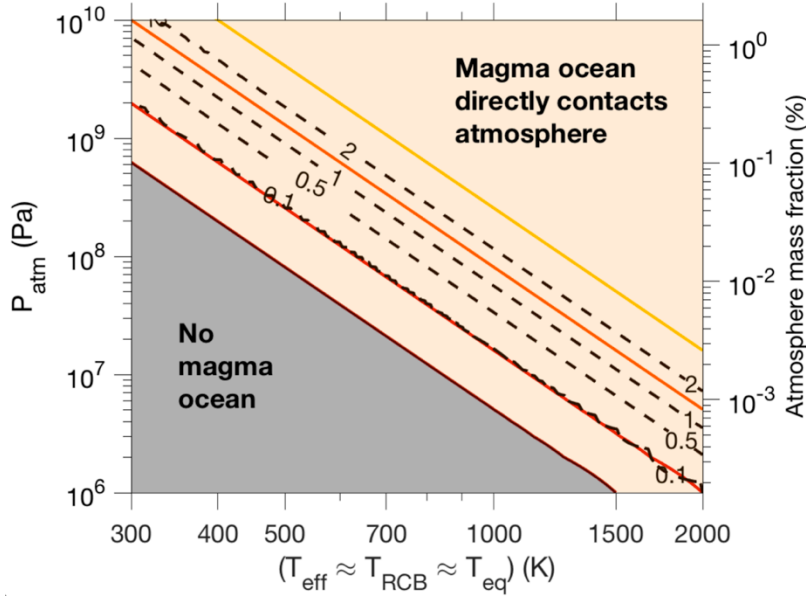


Fig. S1. How magma ocean mass increases with atmospheric thickness. Output from a toy model of sub-Neptune thermal structure (Kite et al. 2020). Dashed lines correspond to magma ocean mass, labeled in Earth-masses of magma, for a volatile-free planet mass of $6 M_{\oplus}$. Colored lines correspond to temperatures at the magma-atmosphere interface of 1500 K (maroon), 2000 K (red), 3000 K (orange), and 4000 K (yellow). Magma ocean masses in excess of 2 Earth masses are not plotted because this corresponds to a magma pressure range that is not well explored by experiments.

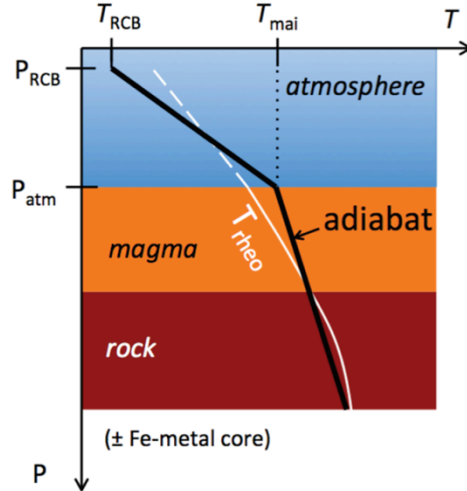


Fig. S2. Planet thermal structure (reproduced from Kite et al., 2020). Temperature versus pressure plot, showing adiabats within the atmosphere and the magma (black line). T_{rheo} (white line) corresponds to the temperature of the rheological transition ($\sim 40\%$ melt fraction) for rock (dashed white line at levels where no rock is present). RCB = radiative-convective boundary. T_{mai} = temperature at the magma-atmosphere interface. For real planets the equilibrium temperature (T_{eq}), the effective temperature (T_{eff}), and the temperature at the RCB (T_{RCB}), are related by $T_{eq} < T_{eff} \lesssim T_{RCB}$. In this paper we make the approximation that these three temperatures are equal (SI Appendix, section 1c).

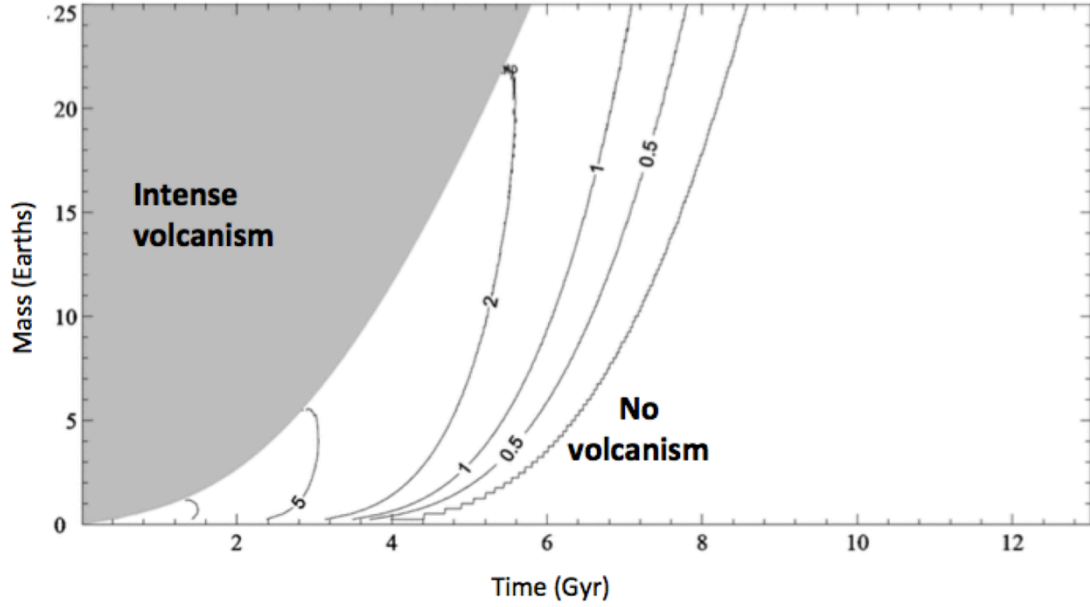


Fig. S3. (Reproduced from Kite et al. 2009, ref. 34 in the main text, by permission of the AAS). Rate of volcanism per unit mass on massive Earth-like planets undergoing stagnant lid convection, normalized to calculated rate on a plate-tectonic Earth, for Katz et al. (2003) melting model. Dark gray shaded regions correspond to mantle temperatures associated with very intense volcanism, too high for a reliable crustal thickness calculation. Contours are at 0, 0.5, 1, 2, 5, and 10 times Earth’s present-day rate of volcanism ($\sim 4 \times 10^{-19} \text{ s}^{-1}$, equivalent to $24 \text{ km}^3 \text{ yr}^{-1}$, in plate-tectonics mode). For example, a $6 M_{\oplus}$ planet on the “2” contour erupts $6 \times 2 \times 24 \approx 300 \text{ km}^3 \text{ yr}^{-1}$.

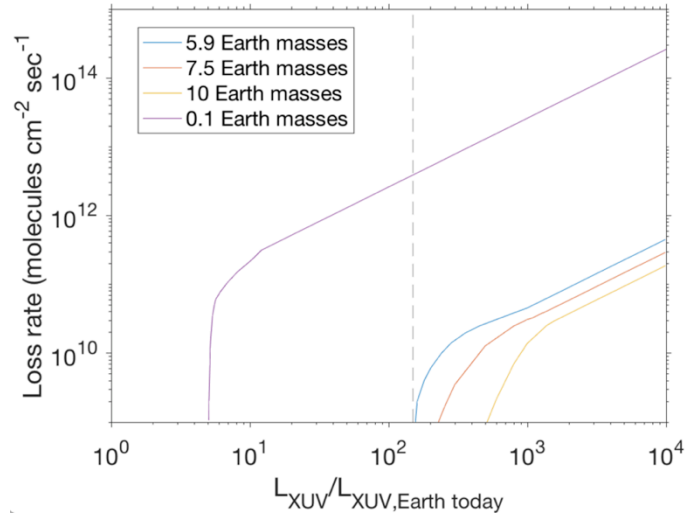


Fig. S4. Atmospheric loss rate for a pure CO_2 atmosphere, combining results for super-Earths (Tian 2009) and for Mars (Tian et al. 2009, scaled to 1 AU). The vertical dashed line corresponds to $150\times$ Earth’s present-day XUV flux.

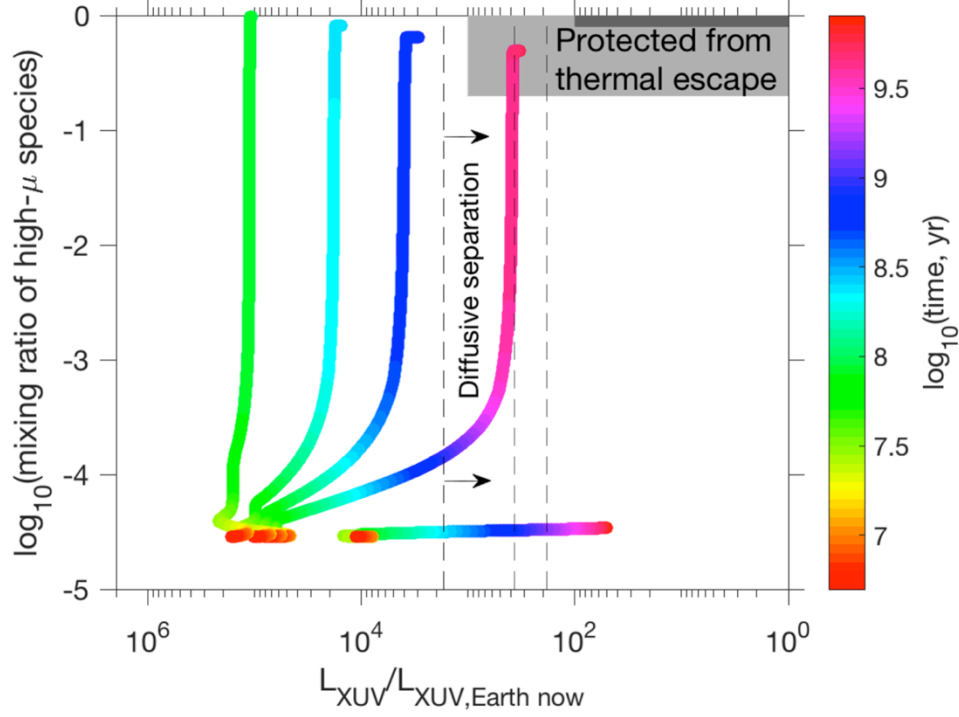


Fig. S5. The same evolutionary tracks as in Fig. 5 (main text), shown in $F_{XUV} - \mu_{avg}$ coordinates. F/F_{\oplus} increases from rightmost track ($F/F_{\oplus} = 49$, $T_{eq} = 735$ K) to leftmost track ($F/F_{\oplus} = 720$, $T_{eq} = 1440$ K). The dashed lines highlight (from right to left) the threshold of F_{XUV} below which all of the high-molecular-mass species is retained by the planet; the F_{XUV} corresponding to a 50% reduction in the no-fractionation loss rate of the high-molecular-mass species; and the F_{XUV} corresponding to escape of the high-molecular-mass species at 90% of the rate at which no loss would occur (SI Appendix, section 1g). Right of the rightmost dashed line, fractionation protects the constituents of the secondary atmosphere, and left of the leftmost dashed line, fractionation is much less important. Calculations are done assuming an atomic wind of H entraining a 1% mixing ratio of atoms of mass 15 Da.

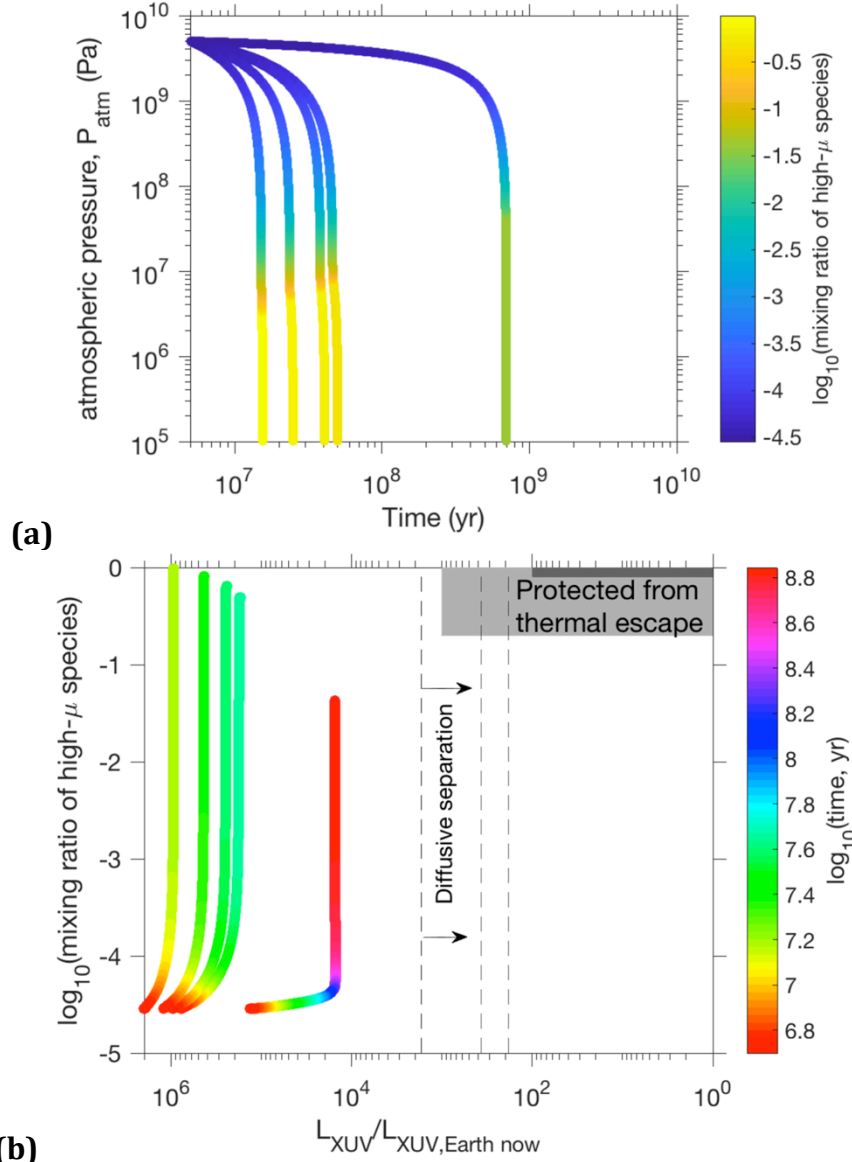


Fig. S6. (a) As Fig. 5a (main text), but for a planet orbiting a star of 0.3 Solar masses. Time-dependent results. Atmospheric pressure vs. time for planets for (from right to left) $F/F_{\oplus} = \{49, 283, 347, 422, 720\}$, corresponding to planet equilibrium temperature ($T_{\text{eq}} = \{735, 1140, 1200, 1275, 1440\}$ K). **(b)** As Fig. S5, but for a planet orbiting a star of 0.3 Solar masses. The same evolutionary tracks as in the top panel, shown in $F_{\text{XUV}} - \mu_{\text{avg}}$ coordinates. F/F_{\oplus} increases from rightmost track ($F/F_{\oplus} = 49$, $T_{\text{eq}} = 735$ K) to leftmost track ($F/F_{\oplus} = 720$, $T_{\text{eq}} = 1440$ K). The dashed lines highlight (from right to left) the threshold of F_{XUV} below which all of the high-molecular-mass species is retained by the planet; the F_{XUV} corresponding to a 50% reduction in the no-fractionation loss rate of the high-molecular-mass species; and the F_{XUV} corresponding to escape of the high-molecular-mass species at 90% of the rate at which no loss would occur (SI Appendix, section 1g). Right of the rightmost dashed line, fractionation protects the constituents of the secondary atmosphere, and left of the leftmost dashed line, fractionation is much less important. Fractionation calculations are done assuming an atomic wind of H entraining a 1% mixing ratio of atoms of mass 15 Da.

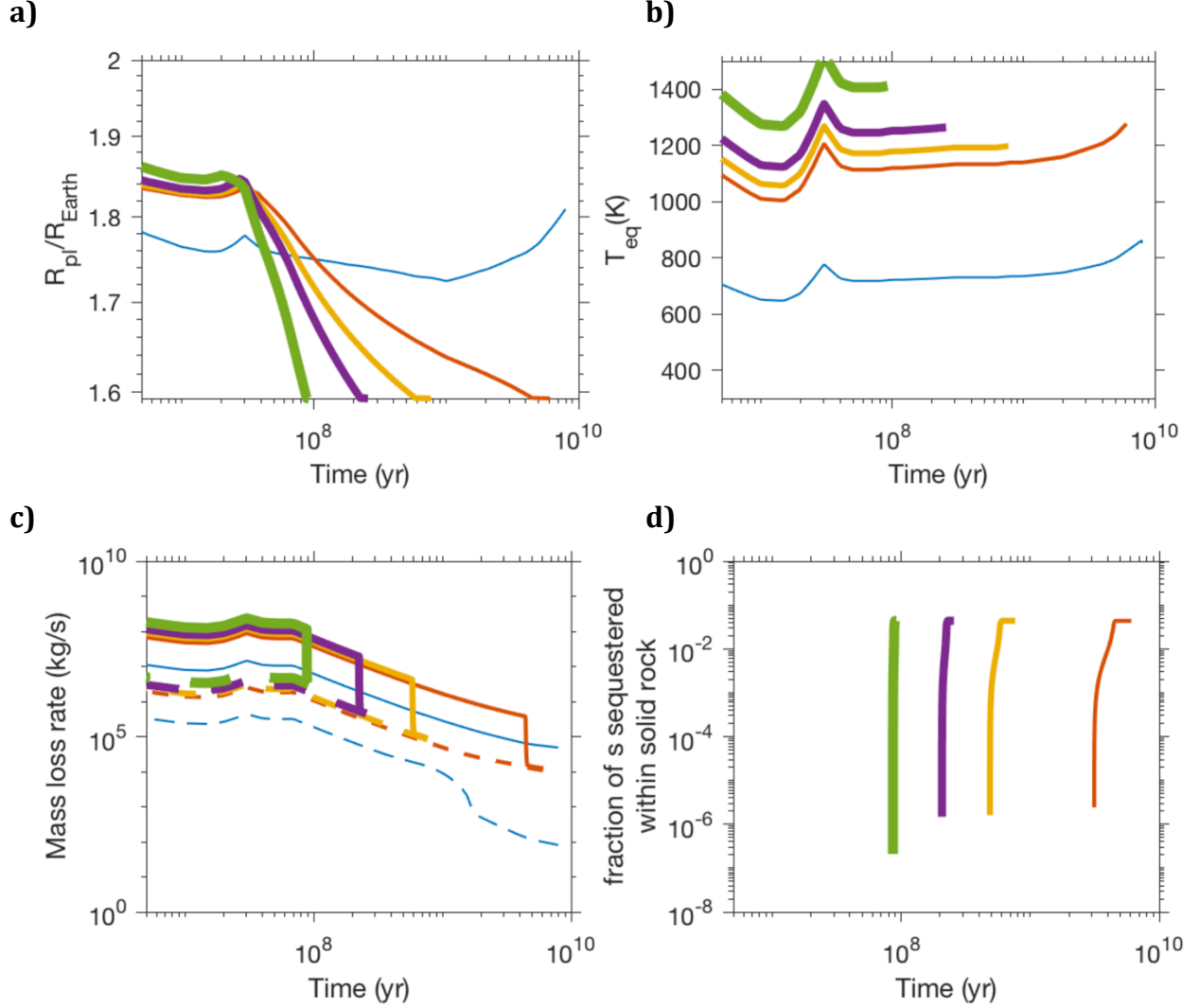


Fig. S7. Details of planet evolution for the tracks shown in Fig. 5a (main text). Solar-mass star, $6 M_{\oplus}$. Line thickness corresponds to insolation, with the thickest lines corresponding to the greatest insolation. Results are shown for $F/F_{\oplus} = 49$ (blue), $F/F_{\oplus} = 283$ (red), $F/F_{\oplus} = 347$ (yellow), $F/F_{\oplus} = 422$ (purple), and $F/F_{\oplus} = 720$ (green), corresponding to $T_{eq} = \{735, 1140, 1200, 1275, 1440\}$ K, respectively. **(a)** Planet radius versus time. **(b)** Planet equilibrium temperature versus time. **(c)** Planet mass loss rate versus time (solid lines), and the mass loss rate that the planet would have if the atmosphere was composed entirely of CO_2 based on the calculations of Tian (2009) (dashed lines). The planets corresponding to the red, yellow, purple, and green lines evolve to a high- μ atmosphere, but only in the red case is this atmosphere long-lived. **(d)** The fraction of the high- μ species (s) that is shielded within solid rock. This is zero for the world that remains as a sub-Neptune (because no solid rock forms), and very similar for the four worlds that transition to super-Earths (full magma crystallization).

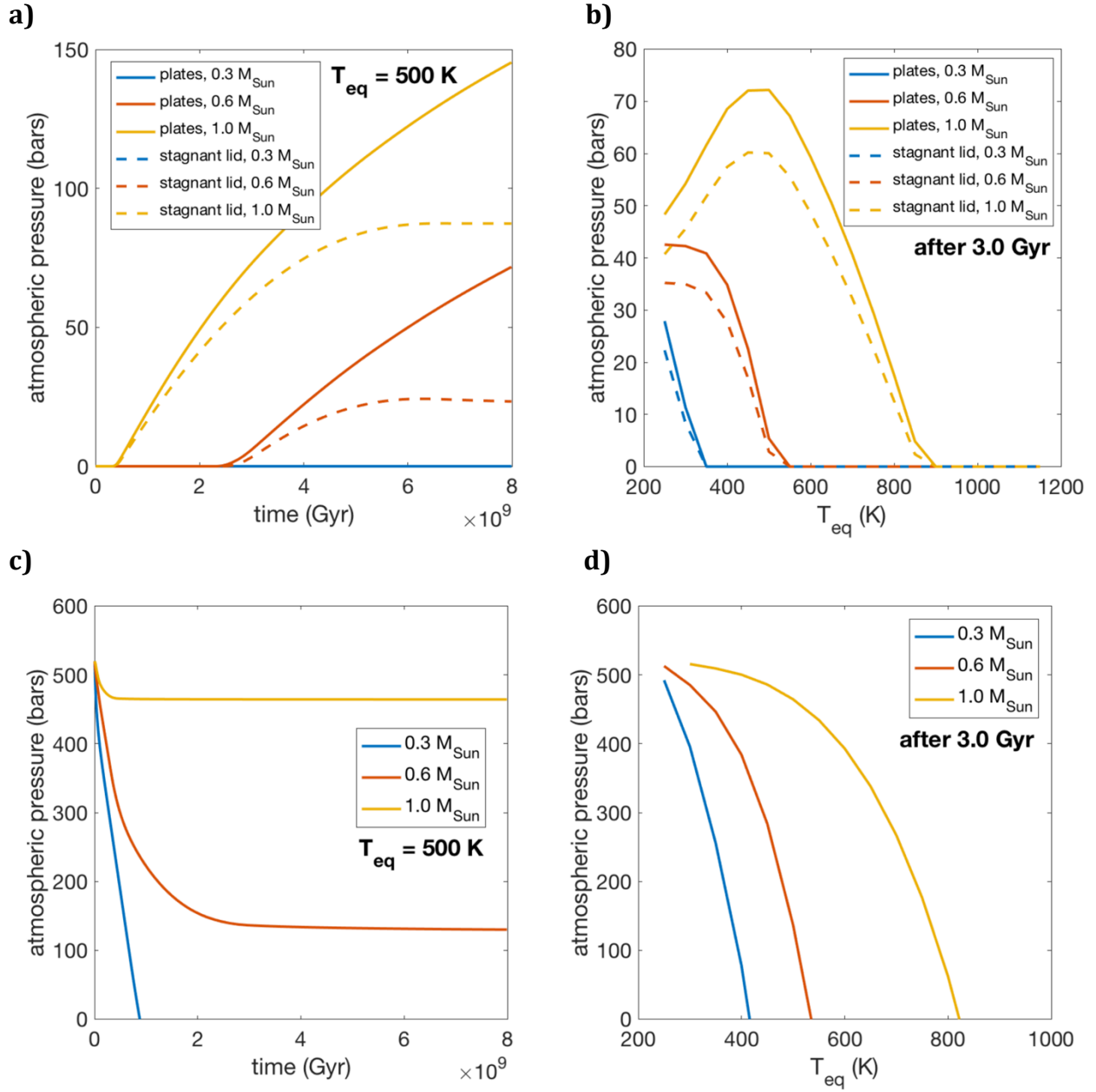


Fig. S8. Atmospheric thickness versus time for the Selsis et al. (2007) XUV model. **(a-b)** volcanic revival, $s_s = 10^{-9} \text{ Pa}^{-1}$, Kite et al. (2009) volcanism model. Results are shown for both plate tectonics (plates), and for stagnant lid mode. There is a minor trend in plate-tectonics mode for planets around Solar-mass stars at $T_{eq} < 500$ K toward decreasing atmospheric thickness with decreasing T_{eq} . This is due to the smaller initial volume of the (*s*-protecting) magma ocean at low T_{eq} . **(c-d)** Start-with-all-volatiles-in-the-atmosphere, residual atmosphere case. In this model, the planet forms with no H_2 (intrinsically rocky) and with 500 bars of *s*, all in the atmosphere.

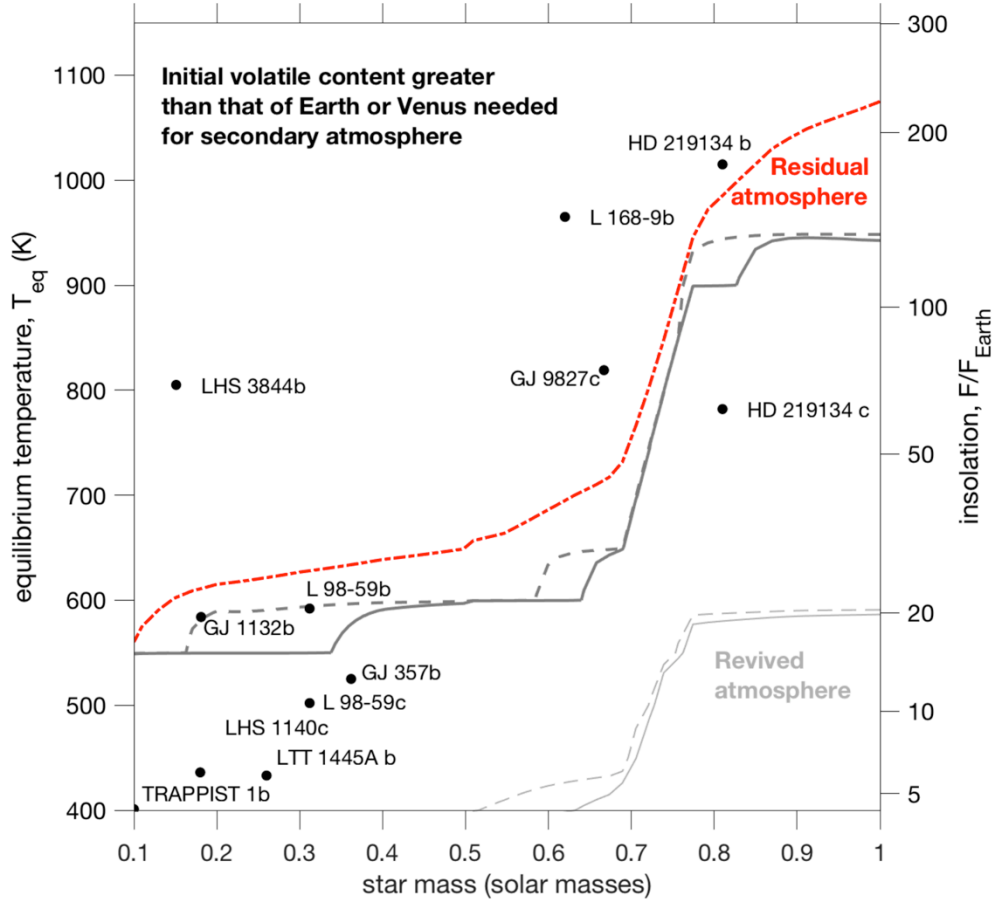


Fig. S9. Deterministic calculation for atmosphere presence/absence after 3.0 Gyr. Deterministic calculation with a fixed XUV flux for each star mass, combining the fits of Jackson et al. (2012) and Guinan et al. (2016). The red dash-dot line corresponds to the line of vanished atmospheres for planets that have all volatiles in the atmosphere initially. Worlds at hotter T_{eq} than this line can retain an atmosphere if there is no H_2 initially and all high-molecular-weight volatiles are in the atmosphere initially. This line moves away from the star over time. The thick gray solid (plate tectonics) and dashed (stagnant lid) lines correspond to the line of atmospheric revival by volcanic outgassing for planets that lose all atmosphere during transition from a sub-Neptune to a super-Earth. These lines of atmospheric revival sweep towards the star over time because the rate of volcanic degassing falls off more slowly with time than does the star's XUV flux. This chart assumes initial volatile supply is independent of F and similar to Earth and Venus. Increasing volatile supply will move thresholds to higher F . The thin gray lines show results for a reduction in the solubility of the high-molecular-weight volatile in the magma from 10^{-9} Pa^{-1} to 10^{-11} Pa^{-1} . Selected exoplanets overplotted. Note that because most of the planets that are shown are too small to have Earth-like composition and $6 M_{\oplus}$, this plot is optimistic for atmospheric survival (higher planet mass favors atmosphere retention). For any individual planet, star-specific XUV-flux estimates, star age, and the planet's mass, should be combined to make a more accurate estimate than is possible using this overview diagram.

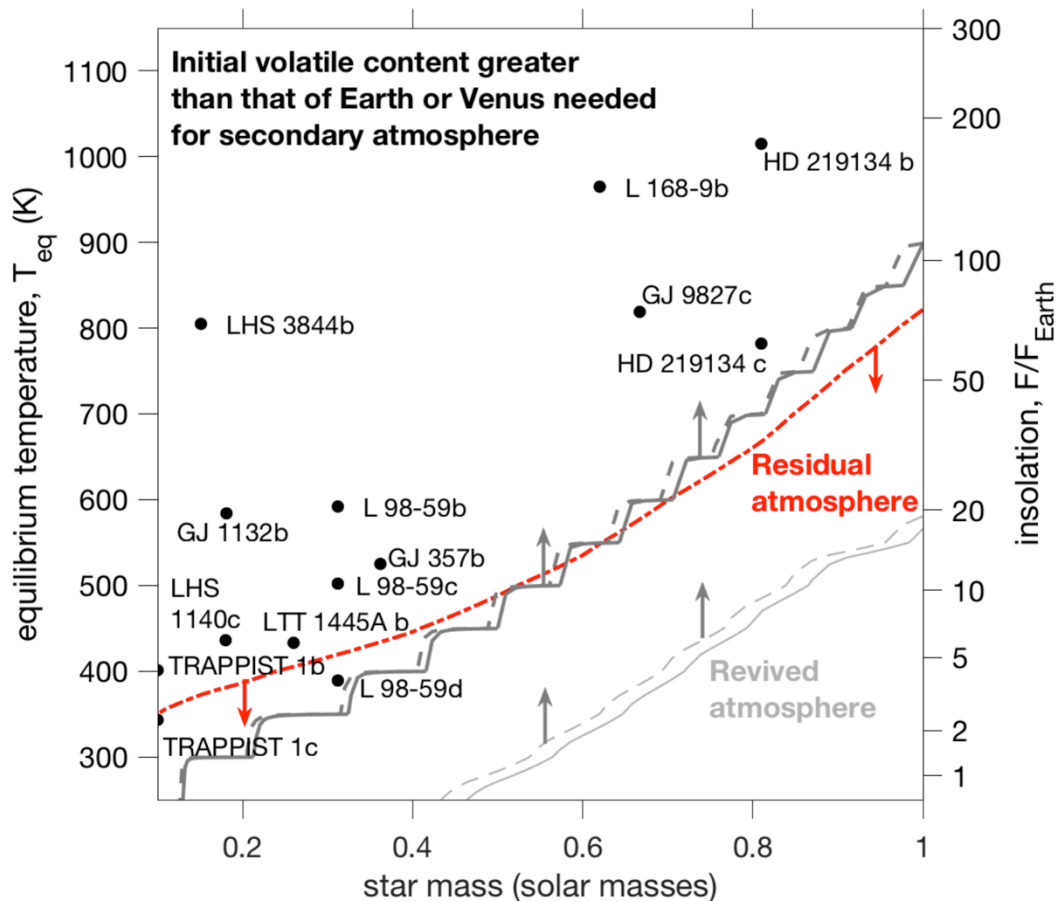


Fig. S10. Deterministic calculation for atmosphere presence/absence after 3.0 Gyr. Deterministic calculation with a fixed XUV flux for each star mass, following Selsis et al. (2007). The red dash-dot line corresponds to the line of vanished atmospheres for planets that have all volatiles in the atmosphere initially. Worlds at hotter T_{eq} than this line can retain an atmosphere if there is no H_2 initially and all high-molecular-weight volatiles are in the atmosphere initially. This line moves away from the star over time (red arrows). The thick gray solid (plate tectonics) and dashed (stagnant lid) lines correspond to the line of atmospheric revival by volcanic outgassing for planets that lose all atmosphere during transition from a sub-Neptune to a super-Earth. These lines of atmospheric revival sweep towards the star over time (gray arrows) because the rate of volcanic degassing falls off more slowly with time than does the star's XUV flux. This chart assumes initial volatile supply is independent of F and similar to Earth and Venus. Increasing volatile supply will move thresholds to higher F . The thin gray lines show results for a reduction in the solubility of the high-molecular-weight volatile in the magma from 10^{-9} Pa^{-1} to 10^{-11} Pa^{-1} . Selected exoplanets overplotted. Note that because most of the planets that are shown are too small to have Earth-like composition and $6 M_{\oplus}$, this plot is optimistic for atmospheric survival (higher planet mass favors atmosphere retention). For any individual planet, star-specific XUV-flux estimates, star age, and the planet's mass, should be combined to make a more accurate estimate than is possible using this overview diagram.

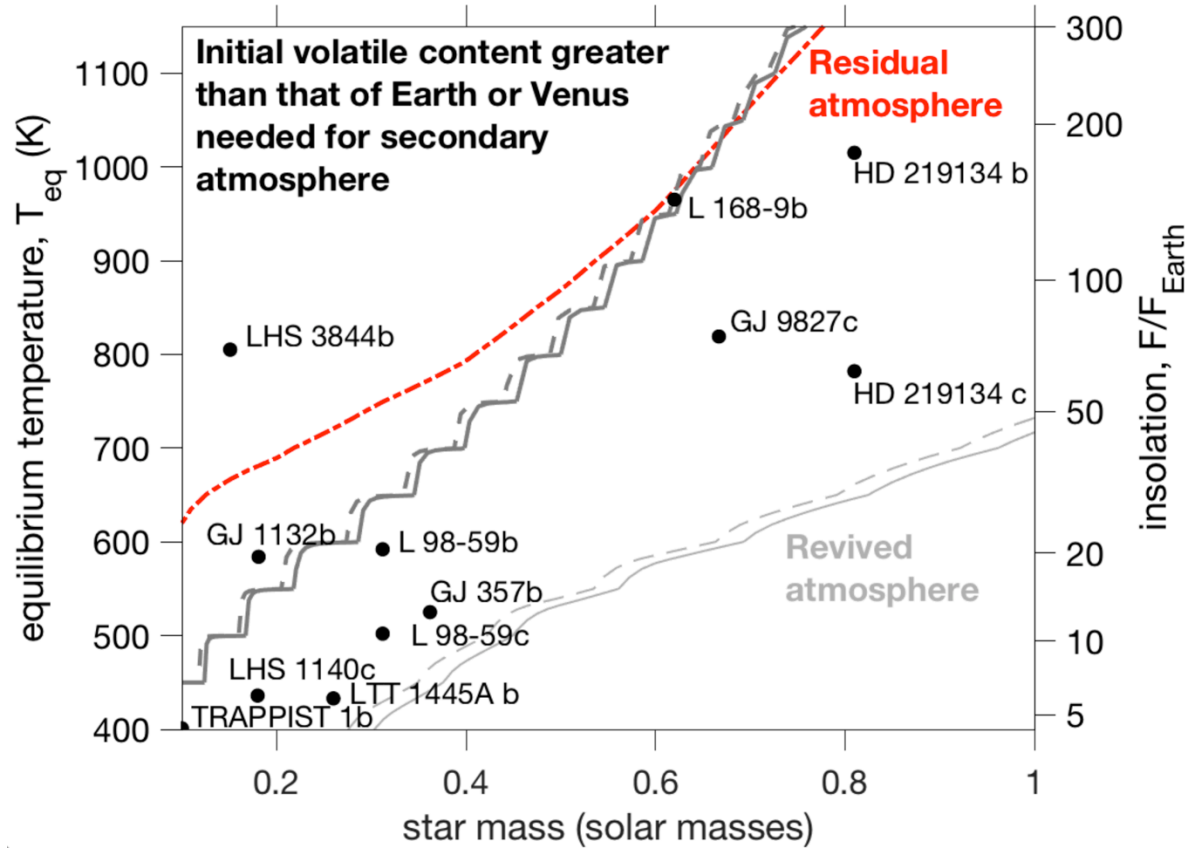


Fig. S11. Small planet atmosphere presence/absence diagram after 3.0 Gyr. As Fig. S10, but with a reduction in XUV flux by a factor of 10, or, equivalently, decreasing the efficiency of XUV-driven loss by a factor of 10, relative to the baseline based on the estimates of Selsis et al. 2007. This increases the range of exoplanets for which a volcanically supported atmosphere is possible. The red dash-dot line corresponds to the line of vanished atmospheres for planets that have all volatiles in the atmosphere initially. Worlds at hotter T_{eq} than this line can retain an atmosphere if there is no H_2 initially and all high-molecular-weight volatiles are in the atmosphere initially. This line moves away from the star over time. The thick gray solid (plate tectonics) and dashed (stagnant lid) lines correspond to the line of atmospheric revival by volcanic outgassing for planets that lose all atmosphere during transition from a sub-Neptune to a super-Earth. The lines of atmospheric revival sweep towards the star over time because the rate of volcanic degassing falls off more slowly with time than does the star's XUV flux. This chart assumes initial volatile supply is independent of F and similar to Earth and Venus. Increasing volatile supply will move thresholds to higher F . The thin gray lines show results for a reduction in the solubility of the high-molecular-weight volatile in the magma from 10^{-9} Pa^{-1} to 10^{-11} Pa^{-1} . Note that because most of the planets that are shown are too small to have Earth-like composition and $6 M_{\oplus}$, this plot is optimistic for atmospheric survival (higher planet mass favors atmosphere retention). For any individual planet, star-specific XUV-flux estimates, star age, and the planet's mass, should be combined to make a more accurate estimate than is possible using this overview diagram.

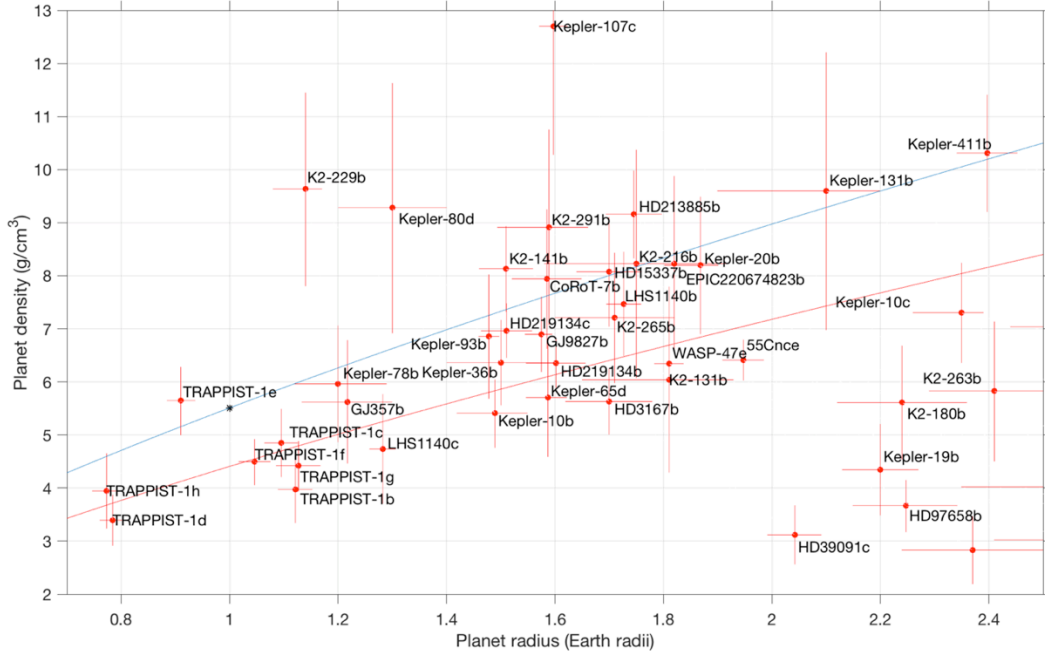


Fig. S12. Planet densities from Otegi et al. (2020). The blue line corresponds to density for Earth-like composition, assuming scaling of mass with planet radius as $(R/R_{\oplus}) = (M/M_{\oplus})^{0.27}$. The red line corresponds to 80% of that density. Many super-Earth sized planets plot below the red line (for example HD 3167 b), indicating either a volatile envelope (atmosphere) or alternatively a very low (Mg+Fe)/Si ratio relative to that of the Earth. Super-Earths with the same or lower density as Earth (e.g. HD 3167 b) are excellent candidates for having elevated-molecular-weight secondary atmospheres. Planets plotting in the low-density, large radius clump in the bottom right are sub-Neptunes, retaining thick H₂-dominated atmospheres.

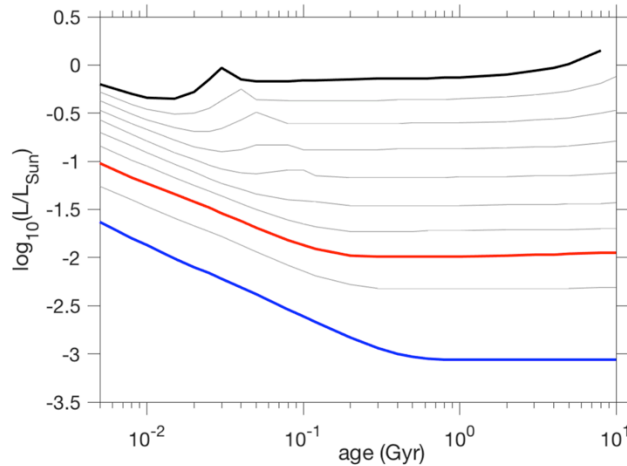


Fig. S13. Stellar luminosity, L , versus time from the model of Baraffe et al. (2015) for star masses ranging from 0.1 – 1.0 M_{\odot} , and normalized to the Sun's luminosity at the present-day (L_{\odot}). Contours drawn at intervals of 0.1 M_{\odot} . The blue line highlights 0.1 M_{\odot} . The red line highlights 0.3 M_{\odot} . The black line highlights 1.0 M_{\odot} .

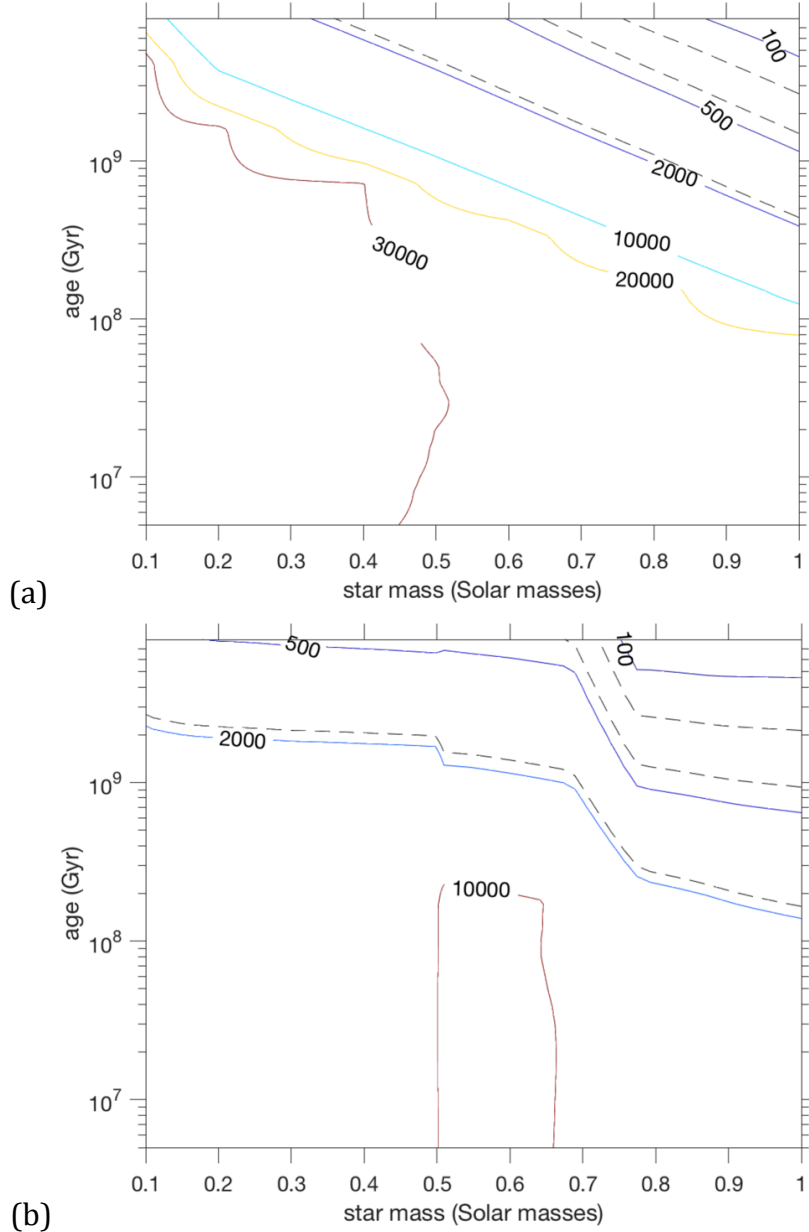


Fig. S14. F_{XUV} at an insolation corresponding to a circular orbit 0.1 AU from today's Sun, in units normalized to the F_{XUV} at Earth's orbit today. (a) for the model of Selsis et al. (2007), and (b) combining the fits of Jackson et al. (2012) and Guinan et al. (2016). The dashed lines highlight (from top to bottom) the threshold of F_{XUV} below which all of the high-molecular-mass species is retained by the planet; the F_{XUV} corresponding to a 50% reduction in the no-fractionation loss rate of the high-molecular-mass species; and the F_{XUV} corresponding to escape of the high-molecular-mass species at 90% of the rate at which no loss would occur. Above the top dashed line, fractionation protects the constituents of the secondary atmosphere, and below the lowest dashed line, fractionation is much less important. Calculations are done assuming an atomic wind of H entraining a 1% mixing ratio of atoms of mass 15 Da, and planet mass $6 M_{\oplus}$.

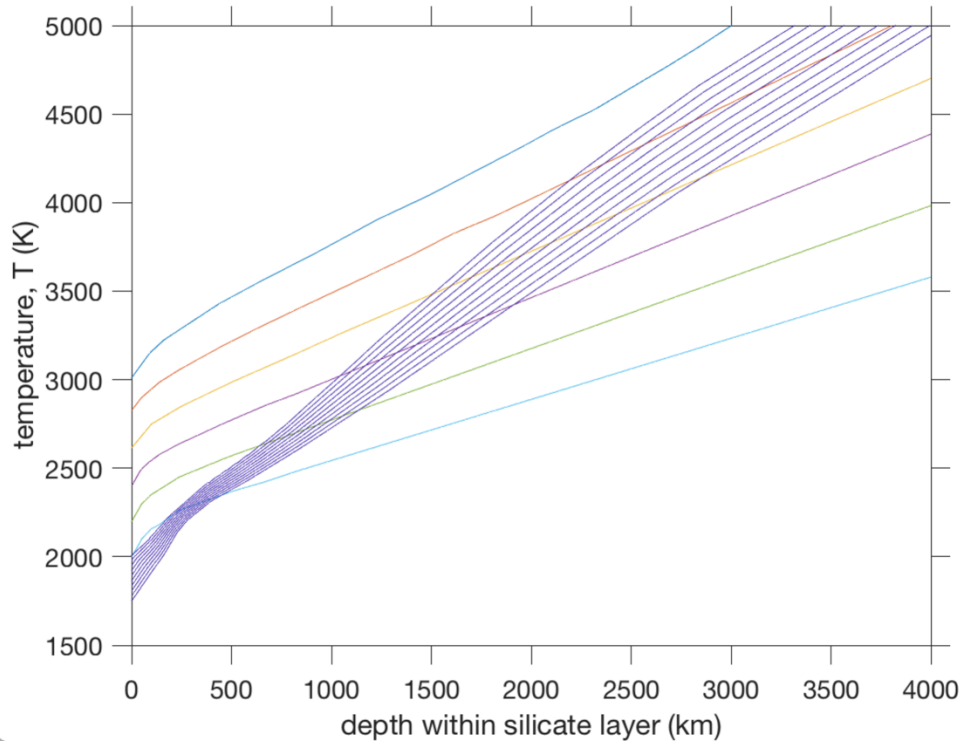


Fig. S15. Andrault et al. (2011) melt curves. Colored lines are magma adiabats (note that these are only physically meaningful for molten magma, i.e. for temperatures higher than the blue lines). Blue lines are melt fraction curves, where the lowest one is the solidus. We find that the effect of atmospheric overburden pressure on the solidus temperature is relatively small. X axis corresponds to depth within a hypothetical Earth-mass planet (the curves correspond to lines in P-T space, so they map to smaller depth on higher-gravity worlds).

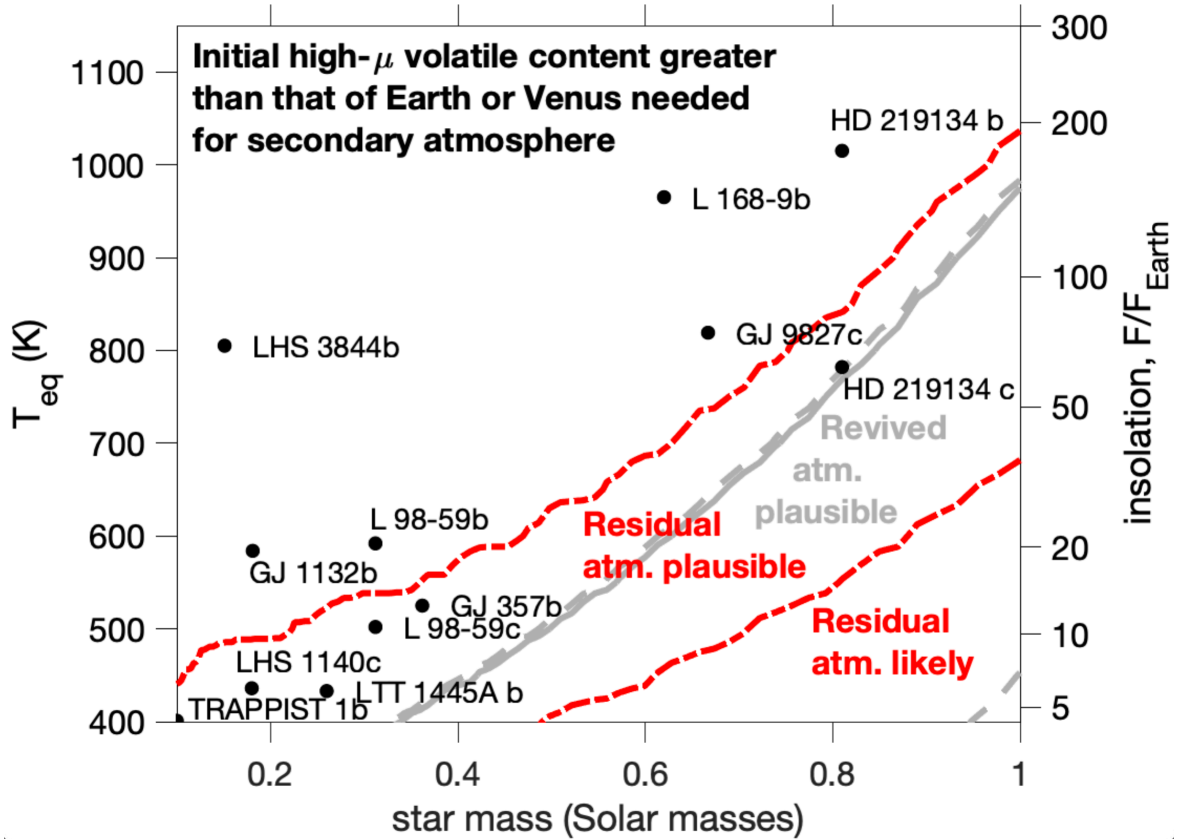
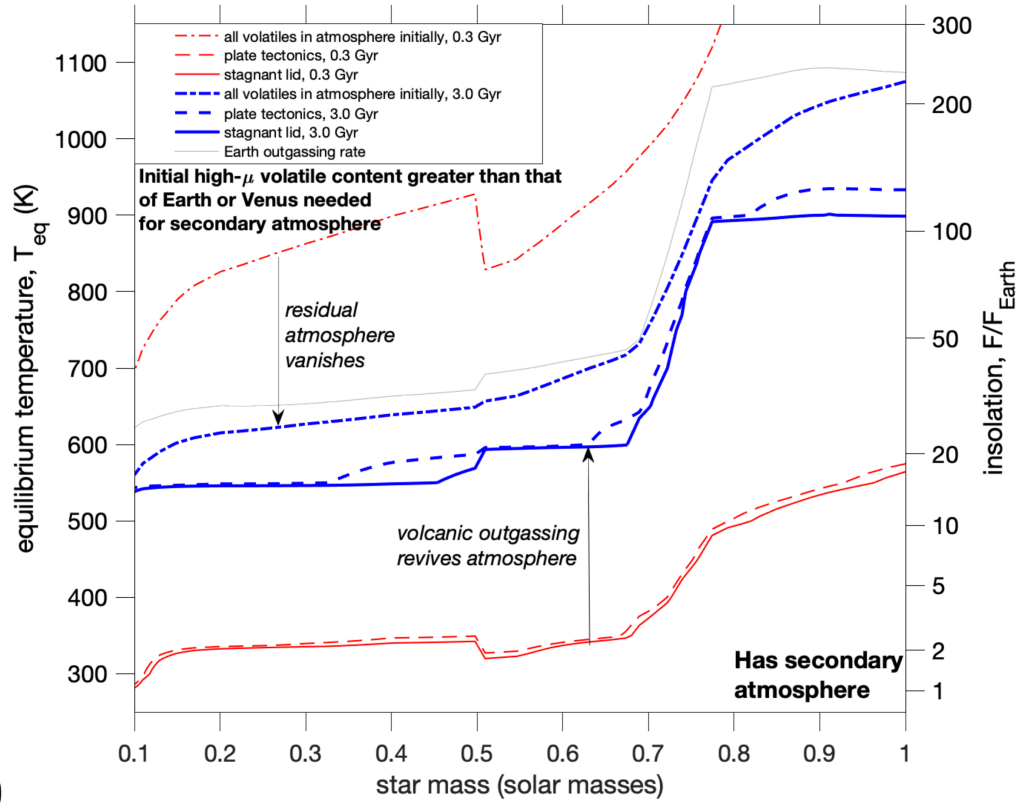
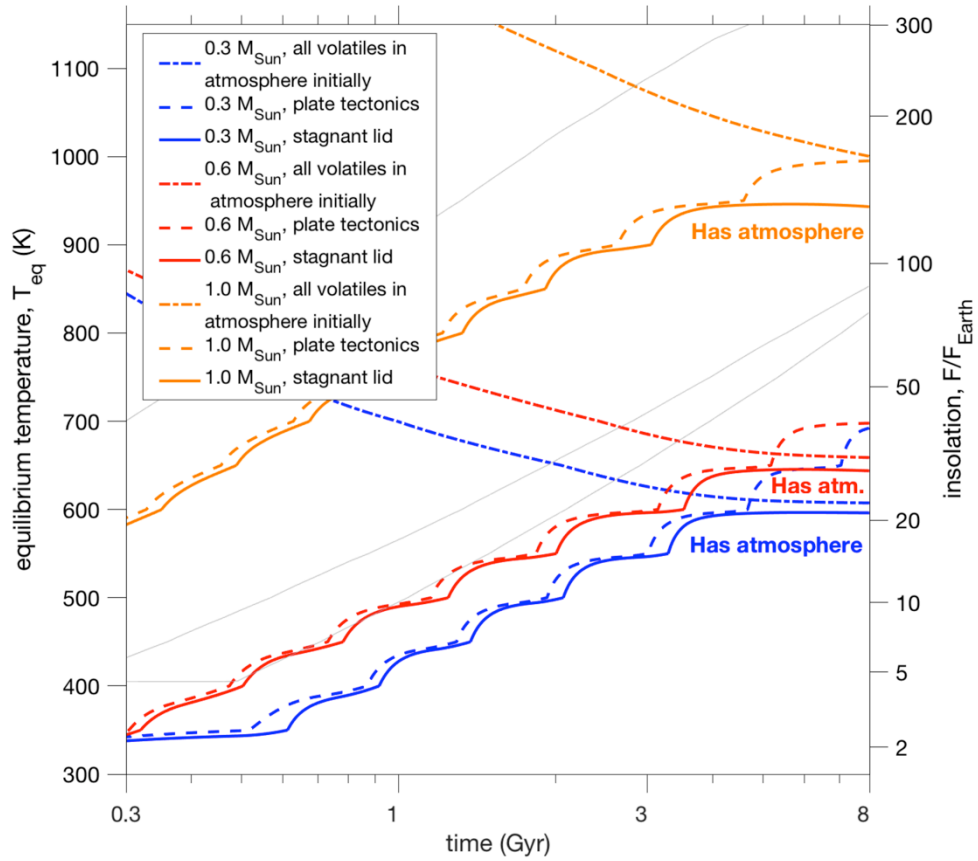


Fig. S16. As Fig. 6 (main text), substituting in an XUV-flux-vs.-time parameterization following Selsis et al. (2007). Secondary atmosphere presence/absence model output for $6 M_{\oplus}$ (higher planet mass favors atmosphere retention). The dashed red lines show the lines of atmosphere retention after 3.0 Gyr for the case where all volatiles are in the atmosphere initially and there is no primary atmosphere; the 16th and 84th percentiles are shown, for varying XUV flux (by ± 0.4 dex, 1σ ; Loyd et al. 2020) relative to the baseline model following the results of Jackson et al. (2012) and Guinan et al. (2016) (SI Appendix, section 1a). These lines move away from the star over time. The gray lines show the 16th percentile for exhibiting an atmosphere after 3.0 Gyr for the case where volcanic outgassing rebuilds the atmosphere from a bare-rock state (the 84th percentile is at $T_{eq} < 400$ K). The solid gray lines are for stagnant-lid tectonics and the dashed gray lines are for plate tectonics. The lines of atmospheric revival sweep towards the star over time because the rate of volcanic degassing falls off more slowly with time than does the star's XUV flux. In each case the atmosphere/no-atmosphere threshold is 1 bar. The black symbols show known planets that may be tested for atmospheres using JWST (Koll et al. 2019, Mansfield et al. 2019). For any individual planet, star-specific XUV-flux estimates, star age, and the planet's mass, should be combined to make a more accurate estimate than is possible using this overview diagram.



(a)



(b)

Fig. S17. (a) Secondary atmosphere presence/absence diagrams for $6 M_{\oplus}$ (higher planet mass favors atmosphere retention). The dash-dot lines correspond to the line of atmosphere vanishing for planets that have all volatiles in the atmosphere initially. The solid and dashed lines correspond to the line of atmospheric revival by volcanic outgassing for planets that lose all atmosphere during transition from a sub-Neptune to a super-Earth. The line of revival sweeps towards the star over time because the rate of volcanic degassing falls off more slowly with time than does the star's XUV flux. The locations of these curves change depending on model assumptions. Increasing volatile supply will move thresholds to higher L . Allowing volatile supply to increase with decreasing T_{eq} , which is realistic, will steepen gradients with L . The gray line is for a constant Earth-scaled outgassing rate (72 bars/Gyr for $6 M_{\oplus}$). **(b).** As (a), but showing changes over time. The gray lines are for 72 bars/Gyr outgassing at different star masses; from top to bottom, $\{0.3, 0.6, 1.0\} M_{\odot}$.